

Article

Shape-Preserved CoFeNi–MOF/NF Exhibiting Superior Performance for Overall Water Splitting across Alkaline and Neutral Conditions

Yu Liu, Panpan Li, Zegao Wang  and Liangjuan Gao * 

College of Materials Science and Engineering, Sichuan University, Chengdu 610065, China; 2021223010040@stu.scu.edu.cn (Y.L.); panpanli@scu.edu.cn (P.L.); zegao@scu.edu.cn (Z.W.)

* Correspondence: lgao87@scu.edu.cn

Abstract: This study reported a multi-functional $\text{Co}_{0.45}\text{Fe}_{0.45}\text{Ni}_{0.9}$ –MOF/NF catalyst for oxygen evolution reaction (OER), hydrogen evolution reaction (HER), and overall water splitting, which was synthesized via a novel shape-preserving two-step hydrothermal method. The resulting bowknot flake structure on NF enhanced the exposure of active sites, fostering a superior electrocatalytic surface, and the synergistic effect between Co, Fe, and Ni enhanced the catalytic activity of the active site. In an alkaline environment, the catalyst exhibited impressive overpotentials of 244 mV and 287 mV at current densities of 50 mA cm^{-2} and 100 mA cm^{-2} , respectively. Transitioning to a neutral environment, an overpotential of 505 mV at a current density of 10 mA cm^{-2} was achieved with the same catalyst, showing a superior property compared to similar catalysts. Furthermore, it was demonstrated that $\text{Co}_{0.45}\text{Fe}_{0.45}\text{Ni}_{0.9}$ –MOF/NF shows versatility as a bifunctional catalyst, excelling in both OER and HER, as well as overall water splitting. The innovative shape-preserving synthesis method presented in this study offers a facile method to develop an efficient electrocatalyst for OER under both alkaline and neutral conditions, which makes it a promising catalyst for hydrogen production by water splitting.

Keywords: electrocatalysis; hydrogen evolution reaction (HER); oxygen evolution reaction (OER); overall water splitting; metal–organic framework (MOF); alkaline and neutral conditions



Citation: Liu, Y.; Li, P.; Wang, Z.; Gao, L. Shape-Preserved CoFeNi–MOF/NF Exhibiting Superior Performance for Overall Water Splitting across Alkaline and Neutral Conditions. *Materials* **2024**, *17*, 2195. <https://doi.org/10.3390/ma17102195>

Academic Editors: Jiayuan Yu and Junfeng Chen

Received: 25 March 2024

Revised: 25 April 2024

Accepted: 26 April 2024

Published: 7 May 2024



Copyright: © 2024 by the authors. Licensee MDPI, Basel, Switzerland. This article is an open access article distributed under the terms and conditions of the Creative Commons Attribution (CC BY) license (<https://creativecommons.org/licenses/by/4.0/>).

1. Introduction

In recent years, environmental issues, especially the greenhouse effect due to fossil fuel combustion, have garnered substantial attention since environmental conservation has significantly intensified [1]. Therefore, the paradigm is shifting from reliance on non-renewable sources to a broader acceptance of clean, renewable energies, such as solar energy, wind energy, hydrogen energy, geothermal energy, and so on. Among these, hydrogen energy stands out as a sustainable and environmentally benign energy carrier [2]. Fuel cell is one of the most effective means to utilize hydrogen, which directly converts chemical energy into electricity at a remarkably high efficiency without generating any pollution in the whole process, ensuring zero environmental contamination [3]. However, the cost of hydrogen production is one of the reasons that impedes the practical application of fuel cells [4,5]. Therefore, seeking a cost-effective method to produce hydrogen at a large scale is imperative. Water electrolysis is considered as one of the most effective solutions to produce hydrogen since water is abundant on Earth in rivers and seas [6,7]. In addition, the electricity generated by solar cells/power and wind could be used as the source of electricity to drive the water electrolysis, which would mitigate the depletion of fossil fuels and reduce the emission of CO_2 to the environment [8–10]. However, an overpotential is required during water electrolysis, which means that the potential required for water electrolysis is higher than the thermodynamic standard potential (1.23 V) due to interfacial resistance, concentration polarization, etc. [11,12]. Thus, the design and preparation of

an efficient electrocatalyst to minimize the overpotential during the water electrolysis has attracted great attention.

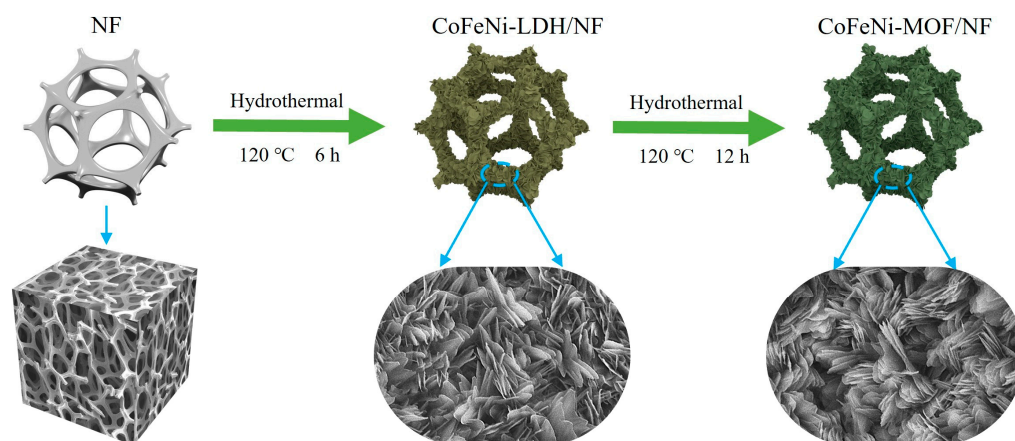
Nowadays, water electrolysis under alkaline environments has been commercialized to produce hydrogen due to several advantages. Predominantly, the lower overpotential under alkaline conditions allows for operation at higher current densities, resulting in the reduction in energy consumption and lifespan extension of the electrolysis equipment, thereby ensuring efficient and stable hydrogen production [13]. Secondly, the restriction on catalyst materials under alkaline conditions is not as stringent as that under acidic conditions. Many non-precious metals such as transition metals and their oxides could be used as potential alkaline water electrolysis catalysts, reducing the application cost of catalysts [14]. Thirdly, the electrolytic tank of alkaline water splitting has a simple structure and low cost because it does not need expensive components such as proton exchange membranes [15]. However, the corrosion of catalysts under alkaline conditions has directed the attention of water electrolysis towards neutral conditions in recent years. Neutral solutions are appealing due to their straightforward preparation, reduced risks, and environmental compatibility [16]. Yet, challenges persist, including a sluggish mass transfer rate, lower current densities, elevated overpotentials, compromised stability, and durability, along with limited comprehension of the reaction mechanisms and kinetics under neutral conditions [17]. In essence, developing a more efficient, durable, and cost-effective electrocatalyst holds profound implications for advancing hydrogen production via water electrolysis, particularly under alkaline and neutral conditions [18].

Metal-organic frameworks (MOFs) represent an emerging class of materials, which possess a stable porous architecture by linking metal atoms with organic ligands via covalent bonds and other interactions [19]. Distinct from traditional materials, MOFs captivate attention due to their low density, extensive specific surface area, and wealth of metal active centers [20]. However, their suboptimal electrical conductivity and inherent catalytic activity have curtailed their potential application in catalytic regions. Therefore, researchers developed preparation strategies such as synergistic effect [21,22], morphology control [23], structure engineering [24], defect engineering [22,25], etc. to make MOF-based catalysts more adaptable to the catalysis of OER and HER. In addition, heterometallic catalysis has been studied extensively [26]. The synergistic effect between heterometallic cations also provides a new idea for the preparation of MOF catalysts [21,27]. For example, Cheng et al. prepared nanobox-like CoCu-MOF through successive cation and ligand exchange strategies, and the synergistic effect between different metal elements and the enhanced active site exposure make it obtain excellent OER performance and stability [28]. Tan et al. loaded ultrafine Ni particles into MOF by partial carbonization, and the rod-like morphology increased the electrochemical active area and the number of active sites of the catalyst. The addition of Ni provides a synergistic effect, enhancing the electrical conductivity of MOF, and enabling HER catalysis in alkaline media to drive a current density of 10 mA cm^{-2} with an overpotential of only 131 mV [29]. Ni-MOF has excellent catalytic activity and electrochemical durability as an electrocatalyst material. However, the overpotential of monomeric MOFs is not satisfactory for rapidly driving OER processes [30,31]. Sun et al. synthesized Fe-doped NiCo-MOF (Fe-NiCo-MOF/NF) by solvothermal method. The changed coordination surroundings changed the local electronic structures of Ni and Co, which could improve the catalytic performance. Because of the enhanced intrinsic activity by the synergistic effect of heterometallic cations, the Fe-NiCo-MOF/NF needs only an overpotential of 290 mV to reach 50 mA cm^{-2} for OER [32].

At present, the one-step hydrothermal method and annealing are commonly used to synthesize MOF-based catalysts. However, the morphology of MOFs obtained by these methods might not meet experimental expectations, resulting in the overuse of raw materials and delays in the development of new catalysts [33,34]. For example, Deng et al. synthesized Ni-MOF by the simple one-step hydrothermal method. However, the generated Ni-MOF exhibits a stratified but randomly oriented morphology, which might result in a low specific surface area and few active sites, thus damaging the catalytic properties

of MOF [35]. At the same time, few existing MOF-based catalysts have been shown to exhibit excellent overall water splitting performance, especially for catalytic applications across neutral and alkaline conditions. Therefore, it is important to develop effective strategies to synthesize MOF-based electrocatalysts for making use of the advantages of MOF structures and improve the overall performance of such catalysts under both neutral and alkaline conditions.

In this study, we synthesized MOF-based electrocatalysts, incorporating metal ions of Co, Fe, and Ni, via the shape-preserving hydrothermal method, which exhibited high catalytic activity. Scheme 1 shows the illustration of the fabrication strategy and process from layered double hydroxide (LDH) to MOF. Remarkably, benefitting from the excellent catalytic activity brought by the synergistic effect of Co, Fe, and Ni cations and the abundant active sites provided by the unique bowknot flake structure, an overpotential of only 287 mV was required to achieve a current density of 100 mA cm^{-2} for OER under 1 M KOH condition, while only 164 mV for HER at a current density of 10 mA cm^{-2} when the CoFeNi-MOF/NF catalyst was used. Under 1 M PBS condition, the overpotentials required for OER and HER at a current density of 10 mA cm^{-2} were 505 mV and 241 mV, respectively. To simulate industrial conditions, a two-electrode electrolytic cell was assembled to evaluate the comprehensive electrolysis performance of CoFeNi-MOF/NF, which demonstrated that such a catalyst exhibited notable catalytic activity. Furthermore, the performance of the catalyst did not degrade significantly across the full process, showing high catalytic stability. This study has provided an effective strategy for designing and crafting innovative bifunctional catalysts that are suitable for diverse environments.



Scheme 1. Schematic illustration of the fabrication process for CoFeNi-MOF/NF.

2. Experimental

2.1. Materials

Ethanol ($\text{C}_2\text{H}_5\text{OH}$, AR), hydrochloric acid (HCl , AR), nickel nitrate hexahydrate ($\text{Ni}(\text{NO}_3)_2 \cdot 6\text{H}_2\text{O}$, AR), iron nitrate nonahydrate ($\text{Fe}(\text{NO}_3)_3 \cdot 9\text{H}_2\text{O}$, AR), cobalt nitrate hexahydrate ($\text{Co}(\text{NO}_3)_2 \cdot 6\text{H}_2\text{O}$, AR), ammonium fluoride (NH_4F , AR), urea ($\text{CO}(\text{NH}_2)_2$, AR), N, N-dimethylformamide (DMF, AR), di-potassium hydrogen phosphate trihydrate ($\text{K}_2\text{HPO}_4 \cdot 3\text{H}_2\text{O}$, AR), and potassium dihydrogen phosphate (KH_2PO_4 , AR) were purchased from Chengdu Kelong Chemical Co., Ltd. (Chengdu, China). p-Phthalic acid (H_2BDC , 99%) was purchased from Shanghai Aladdin Biochemical Technology Co., Ltd. (Shanghai, China). Potassium hydroxide–water standard titration solution (KOH 1.0000 mol/L) was purchased from Guangzhou Howei Pharma Tech Co., Ltd. (Guangzhou, China). Nickel foam (NF) was purchased from Shenzhen Green and Creative Environmental Science and Technology Co., Ltd. (Shenzhen, China), and was pretreated with HCl, deionized water, and ethanol several times to remove the surface impurities.

2.2. Preparation of CoFeNi–LDH/NF

Typically, 0.45 mmol $\text{Fe}(\text{NO}_3)_2 \cdot 9\text{H}_2\text{O}$, 0.9 mmol $\text{Ni}(\text{NO}_3)_2 \cdot 6\text{H}_2\text{O}$, 0.45 mmol $\text{Co}(\text{NO}_3)_2 \cdot 6\text{H}_2\text{O}$, 3 mmol NH_4F , and 6 mmol urea were dissolved into 80 mL deionized water and stirred for 15 min. Then, the solution was transferred into a 100 mL Teflon-lined autoclave. A piece of pretreated NF (3 cm \times 4 cm) was immersed into the above solution. The autoclave was then heated at 120 °C for 6 h. After cooling down to room temperature, the sample was washed several times with deionized water and ethanol and then dried at 70 °C for 3 h. The sample was named $\text{Co}_{0.45}\text{Fe}_{0.45}\text{Ni}_{0.9}\text{-LDH/NF}$.

2.3. Preparation of CoFeNi–MOF/NF

In this procedure, 0.45 mmol $\text{Fe}(\text{NO}_3)_2 \cdot 9\text{H}_2\text{O}$, 0.9 mmol $\text{Ni}(\text{NO}_3)_2 \cdot 6\text{H}_2\text{O}$, 0.45 mmol $\text{Co}(\text{NO}_3)_2 \cdot 6\text{H}_2\text{O}$, and 1.35 mmol H_2BDC were dissolved into 70 mL DMF and stirred for 15 min. Then, 5 mL deionized water and 5 mL ethanol were added into the solution and stirred for 10 min. Then, the solution was transferred into a 100 mL Teflon-lined autoclave. The $\text{Co}_{0.45}\text{Fe}_{0.45}\text{Ni}_{0.9}\text{-LDH/NF}$ was immersed into the above solution. The autoclave was then heated at 120 °C for 12 h. After cooling down to room temperature, the sample was washed several times with deionized water and ethanol and then dried at 70 °C for 3 h. For comparison, samples with different dosages of $\text{Co}(\text{NO}_3)_2 \cdot 6\text{H}_2\text{O}$ and $\text{Fe}(\text{NO}_3)_2 \cdot 9\text{H}_2\text{O}$ were prepared using the same procedures.

2.4. Electrochemical Measurement

The electrochemical measurements were conducted on the electrochemical workstation (CHI 660E) with a standard three-electrode system. A graphite electrode was used as the counter electrode. The Hg/HgO and saturated calomel electrode (SCE) were used in 1 M KOH solution and 1 M PBS solution, respectively. CoFeNi–MOF/NF (1 cm \times 1 cm) was used as the working electrode. All potentials reported in this work were converted to reversible hydrogen electrode (RHE) according to the following equations:

$$E_{\text{RHE}} = E_{\text{Hg}/\text{HgO}} + 0.098 \text{ V} + 0.059 \times \text{pH}$$

or

$$E_{\text{RHE}} = E_{\text{SCE}} + 0.244 \text{ V} + 0.059 \times \text{pH}$$

Linear sweep voltammetry (LSV) tests were carried out at the scanning rate of 5 mV s^{-1} , and an iR correction was carried out at 85% to ignore the influence of uncompensated resistance.

2.5. Characterizations

The morphologies of samples were analyzed using a field emission scanning electron microscope (FESEM) SIGMASEM300 (ZEISS, Oberkochen, Germany). Energy Dispersive Spectroscopy (EDS) was performed using Oxford instruments Xplore equipped with FESEM for elemental mapping. Inductively Coupled Plasma Optical Emission Spectrometer (ICP–OES) was performed using 5110 ICP–OES (Agilent, Beijing, China). X–ray diffraction (XRD) were obtained using XRD–6100 (Shimazu, Kyoto, Japan) diffractometer with Cu–K α radiation ($\lambda = 1.5406 \text{ \AA}$) at 40 kV and 30 mA from 5° to 80°. High–resolution transmission electron microscope (HRTEM) was performed using JEM F200 (JEOL, Tokyo, Japan), and the EDS was performed using JED–2300T. X–ray photoelectron spectroscopy (XPS) measurements were performed on a Thermo Scientific K–Alpha photoelectron spectrometer (Thermo Fisher Scientific, Waltham, MA, USA) using Al as the excitation source, and the binding energy peak of C 1s at 284.8 eV was used as a calibration peak.

3. Results and Discussion

Scanning electron microscopy (SEM) images revealed that the samples exhibited consistent growth of bowknot flakes on NF (as shown in Figure 1a), which facilitates a plethora of active sites that are conducive for water splitting. Analogous morphologies of LDH

can be found in Figure S1a, and the larger magnification of $\text{Co}_{0.45}\text{Fe}_{0.45}\text{Ni}_{0.9}\text{-MOF/NF}$ is shown in Figure S1b. In the solvothermal process, Co^{2+} , Ni^{2+} , and Fe^{3+} in the solution first replaced H^+ , which uniformly dispersed on both sides of CoFeNi-LDH , and then acted as the reaction site of MOF self-assembly, transforming all the remaining metallic oxide into a homogeneous MOF phase [35]. The LDH morphologies corroborate the efficacy of the shape-preserving method in synthesizing MOFs, as evidenced by the recurring bowknot flake configuration. Morphological variations with different Co and Fe molar ratios in the MOFs are presented in Figure S2a–d. It is worth highlighting that variations in Co and Fe contents significantly modulate the morphologies of samples. There is a perceptible transition from a dispersed sheet-like structure to a more aggregated columnar one, potentially influencing the exposure level of the active sites. Energy dispersive spectrum (EDS) elemental mapping for $\text{Co}_{0.45}\text{Fe}_{0.45}\text{Ni}_{0.9}\text{-MOF/NF}$ is portrayed in Figure 1b–f, and the accompanying EDS spectra in Figure S3 confirm the uniform distribution of C, O, Ni, Co, and Fe elements within the sample. To further determine the composition of metallic elements in catalyst samples, ICP-OES tests were performed as shown in Table S1. In the synthesis process, NF itself also plays a role as one of the sources of Ni due to the etching of NF during the reaction processes by the solvent. Therefore, the percentage of Ni is much higher than that of Co and Fe, about 75% [36,37]. The metal percentages of Co and Fe are 14.26% and 10.76%, respectively, and this slight difference might be due to differences in the hydrolysis rate of the two cations [38].

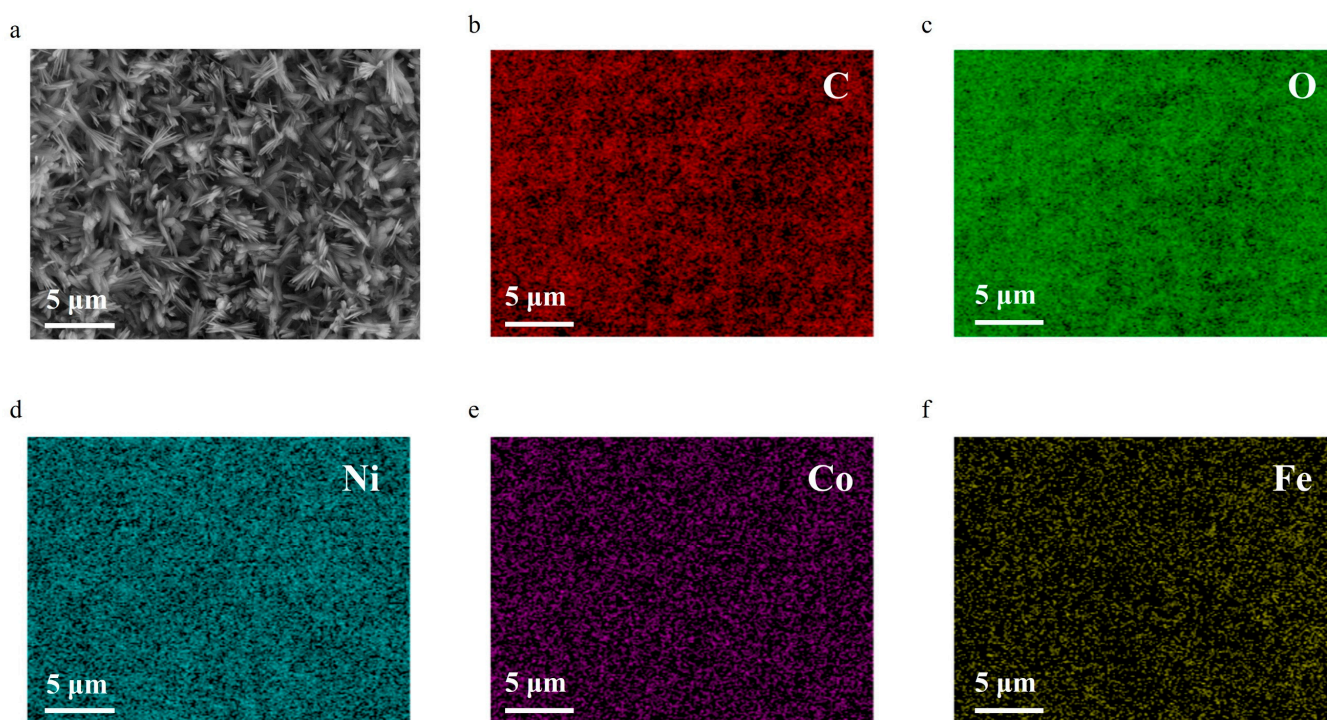


Figure 1. (a) SEM image and (b–f) EDS elemental mapping of $\text{Co}_{0.45}\text{Fe}_{0.45}\text{Ni}_{0.9}\text{-MOF/NF}$.

We subsequently employed X-ray diffraction (XRD) to probe the structural attributes of $\text{Co}_{0.45}\text{Fe}_{0.45}\text{Ni}_{0.9}\text{-LDH}$ powder, $\text{Co}_{0.45}\text{Fe}_{0.45}\text{Ni}_{0.9}\text{-MOF}$ powder, and $\text{Co}_{0.45}\text{Fe}_{0.45}\text{Ni}_{0.9}\text{-MOF/NF}$. As illustrated in Figure 2a, distinct peaks at approximately 2θ of 11.6° , 23.4° , 33.2° , 34.1° , 35.1° , 38.7° , 52.4° , 56.1° , 59.1° , and 60.6° correspond to (0 0 3), (0 0 6), (1 0 1), (0 1 2), (0 0 9), (0 1 5), (1 0 10), (0 1 11), (1 1 0), and (1 1 3) planes of CoFe-LDH ($\text{Co}_{5.84}\text{Fe}_{2.16}(\text{OH})_{16}(\text{CO}_3)_{1.08}\cdot 0.32\text{H}_2\text{O}$ PDF#050–0235) and NiFe-LDH ($\text{Ni}_{5.64}\text{Fe}_{2.36}(\text{OH})_{16}(\text{CO}_3)_{1.18}\cdot 7.52\text{H}_2\text{O}$ PDF#51–0463). In the octahedrally coordinated LDH, metal cations occupy the coordination center, and the apex of the octahedron contains hydroxide ions. During the hydrolysis process, urea was used to adjust the pH value required for the growth of LDH; meanwhile, the formed carbonate ions were supplied as

the intercalation. The cationic charge in the LDH layer is compensated by the presence of hydrated and carbonate anions between the stacked layers [39]. Here, Fe^{3+} and Co^{2+} can replace some of the lattices in $\text{Ni}(\text{OH})_2$ (PDF#73–1520) to form a stable LDH structure, with excess cations balanced by anion intercalation between the hydroxide layers, and eventually generate a uniform LDH compound [27,32,40]. The XRD for $\text{Co}_{0.45}\text{Fe}_{0.45}\text{Ni}_{0.9}\text{-MOF/NF}$ presented in Figure 2b reveals that, due to the pronounced diffraction peaks from the NF substrate, the characteristic peaks of the MOF are not obvious, but still can see a weak peak at 2θ of 8.9° (as shown in the partially enlarged image in Figure 2b). However, the analysis of the powdered samples indicates that peaks at 2θ of 8.9° , 14.9° , 15.7° , and 16.9° are all corresponding to the crystal facets of Ni-MOF (CCDC no. 985792), Co-MOF, and Fe-MOF [41,42]. Importantly, a slight leftward shift from the standard diffraction peaks was observed, signifying that Fe and Co doping induces lattice expansion in the resultant sample [43]. Figure S4 shows the HRTEM and EDS results of $\text{Co}_{0.45}\text{Fe}_{0.45}\text{Ni}_{0.9}\text{-MOF/NF}$. Although XRD results show that we have successfully synthesized the crystal structure, it is difficult to observe the obvious lattice fringes in HRTEM images because the lattice structure of MOF is easily decomposed under the electron beam, as shown in Figure S4a,b [44,45]. Figure S4c–f show the EDS results of $\text{Co}_{0.45}\text{Fe}_{0.45}\text{Ni}_{0.9}\text{-MOF/NF}$, indicating the uniform distribution of Co, Fe, and Ni in the catalyst.

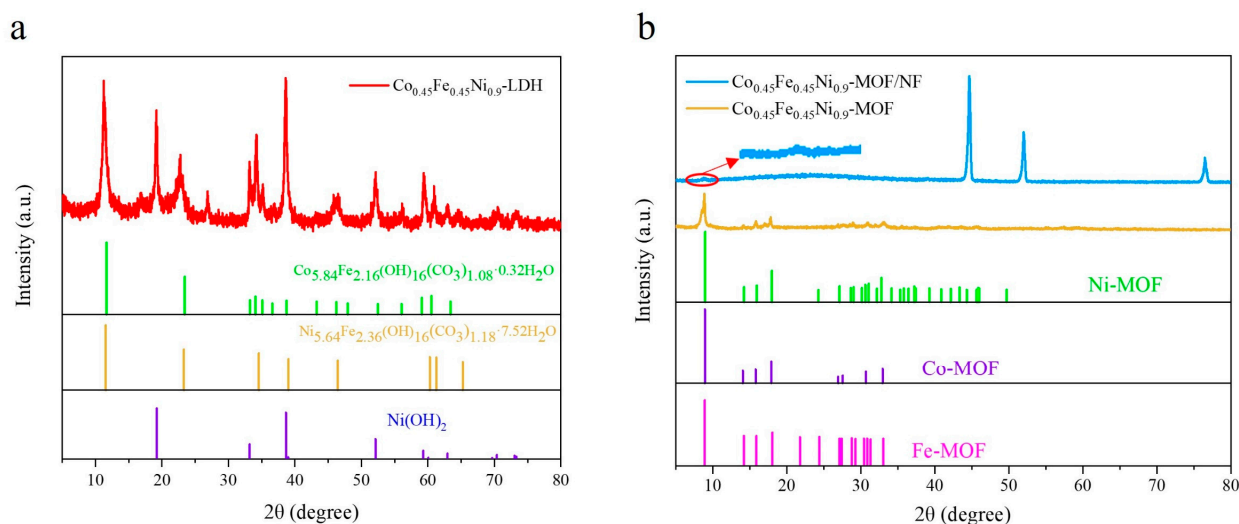


Figure 2. XRD patterns of (a) $\text{Co}_{0.45}\text{Fe}_{0.45}\text{Ni}_{0.9}\text{-LDH}$ and (b) $\text{Co}_{0.45}\text{Fe}_{0.45}\text{Ni}_{0.9}\text{-MOF/NF}$ and $\text{Co}_{0.45}\text{Fe}_{0.45}\text{Ni}_{0.9}\text{-MOF}$. The inset in (b) is corresponding to the magnified XRD data in the red circle for $\text{Co}_{0.45}\text{Fe}_{0.45}\text{Ni}_{0.9}\text{-MOF/NF}$.

X-ray photoelectron spectroscopy (XPS) was employed to delve deeper into the elemental composition and associated chemical states of samples. Figure 3a verifies the existence of C, O, Ni, Fe, and Co elements in $\text{Co}_{0.45}\text{Fe}_{0.45}\text{Ni}_{0.9}\text{-MOF/NF}$, and the Ni 2p peak of $\text{Co}_{0.45}\text{Ni}_{0.9}\text{-MOF/NF}$ is relatively lower than that of $\text{Co}_{0.45}\text{Fe}_{0.45}\text{Ni}_{0.9}\text{-MOF/NF}$ and $\text{Fe}_{0.45}\text{Ni}_{0.9}\text{-MOF/NF}$. XPS peak strength is related to the relative content of elements. However, because the amount of metal salt used in the synthesis process and the element content in the final synthesized catalyst are not the same, the peak strength of the same element in different materials might be different. Moreover, the absence of Fe in $\text{Co}_{0.45}\text{Ni}_{0.9}\text{-MOF/NF}$ reduces the etching of NF by Fe hydrolysis during the synthesis process, which is consistent with what has been reported in the literature [36]. The core-level binding energy (BE) of C 1s in Figure 3b aligns with the carbon-carbon double bond (C=C) at 284.8 eV, associated with the benzene rings from the H_2BDC linker, the C-O polar covalent bond at 286.3 eV, and the carboxylate groups (O-C=O) of the organic ligand at 288.4 eV. The BE diagram of O 1s in Figure 3c displays peaks at 529.5 eV, 531.1 eV, 531.9 eV, and 533.0 eV and are attributed to Metal(M)-O, M-OH, oxygen vacancy, and O-C=O, respectively. The high-resolution spectra of Co 2p, Fe 2p, and Ni 2p split into $2p_{1/2}$

and $2p_{3/2}$ due to spin–orbit coupling. Specifically, for $\text{Co}_{0.45}\text{Fe}_{0.45}\text{Ni}_{0.9}\text{-MOF/NF}$, the Ni 2p spectrum (Figure 3d) reveals peaks at 873.7 eV and 856 eV, corresponding to Ni $2p_{1/2}$ and Ni $2p_{3/2}$. Satellite peaks around these peaks indicate the presence of Ni^{2+} and Ni^{3+} . For Fe 2p (Figure 3e), the binding energies at 724 eV and 712.5 eV are linked to Fe $2p_{1/2}$ and Fe $2p_{3/2}$, with an accompanying satellite peak signifying the existence of both bivalent and trivalent Fe. In the Co 2p spectrum (Figure 3f), peaks at 781.3 eV and 796.9 eV correspond to Co $2p_{1/2}$ and Co $2p_{3/2}$. Satellite peaks surrounding them confirm the presence of both Co^{2+} and Co^{3+} [18,27,32,40,46,47]. Due to the introduction of Fe species, the Co $2p_{3/2}$ peak of $\text{Co}_{0.45}\text{Fe}_{0.45}\text{Ni}_{0.9}\text{-MOF/NF}$ was positively shifted by 0.27 eV, and the Co $2p_{1/2}$ peak was negatively shifted by 0.47 eV compared to $\text{Co}_{0.45}\text{Ni}_{0.9}\text{-MOF/NF}$. Also, because of the introduction of Co species, the Fe $2p_{3/2}$ peak of $\text{Co}_{0.45}\text{Fe}_{0.45}\text{Ni}_{0.9}\text{-MOF/NF}$ was positively shifted by 0.35 eV and the Fe $2p_{1/2}$ peak was negatively shifted by 0.57 eV compared to $\text{Co}_{0.45}\text{Ni}_{0.9}\text{-MOF/NF}$. The above results indicate that the introduction of Fe and Co affected the oxidation states, which may influence the band structure of the elements, and thus would promote the surface charge transfer among elements, resulting in a positive impact on the catalytic effect [48]. Moreover, compared with $\text{Co}_{0.45}\text{Ni}_{0.9}\text{-MOF/NF}$, the Ni 2p of $\text{Co}_{0.45}\text{Fe}_{0.45}\text{Ni}_{0.9}\text{-MOF/NF}$ has a negative shift of 0.27 eV, and the overall analysis shows that the 2p orbitals of Fe and Co also have different degrees of negative shift, indicating that the presence of high–valence Co, Fe, and Ni increases, which also has a positive effect on the water decomposition reaction [49]. By comparing the semi–quantitative peak area, it is found that the proportion of $\text{Co}^{3+}/\text{Co}^{2+}$ in $\text{Co}_{0.45}\text{Fe}_{0.45}\text{Ni}_{0.9}\text{-MOF/NF}$ is about 10% higher than that in $\text{Co}_{0.45}\text{Ni}_{0.9}\text{-MOF/NF}$. Considering the sequence of ionic electronegativity (Co^{2+} (9.10) < Ni^{2+} (9.60) < Fe^{3+} (15.38)), the introduction of Fe can attract electrons of Co and Ni, thereby improving the adsorption and desorption ability of intermediate products in the catalytic process [40,50,51].

The OER performance of $\text{Co}_{0.45}\text{Fe}_{0.45}\text{Ni}_{0.9}\text{-MOF/NF}$ was assessed within a three–electrode system containing a 1 M KOH solution. Evaluations against samples with varying Co and Fe doping concentrations substantiated that the catalyst achieved peak activity when both Co and Fe were maintained at 0.45 mmol. For comparative insights, $\text{Fe}_{0.45}\text{Ni}_{0.9}\text{-MOF/NF}$ and $\text{Co}_{0.45}\text{Ni}_{0.9}\text{-MOF/NF}$ were analyzed under identical conditions. It can be seen from Figure 4a that $\text{Co}_{0.45}\text{Fe}_{0.45}\text{Ni}_{0.9}\text{-MOF/NF}$ exhibits superior OER efficacy compared to other catalysts. The OER overpotentials were only 244 mV at 50 mA cm^{-2} and 287 mV at 100 mA cm^{-2} , respectively. However, $\text{Fe}_{0.45}\text{Ni}_{0.9}\text{-MOF/NF}$ and $\text{Co}_{0.45}\text{Ni}_{0.9}\text{-MOF/NF}$ require higher overpotentials of 260 mV and 330 mV at the current density of 50 mA cm^{-2} and 300 mV and 373 mV at the current density of 100 mA cm^{-2} , respectively. Both NF and MOFs contain Ni elements, in order to prove whether the active sites of Ni in NF or the MOFs improves the catalytic activity, we compared the catalytic performance of bare NF and MOFs. The results showed that the overpotential of MOFs was much lower than that of NF (448 mV @ 50 mA cm^{-2} , 491 mV @ 100 mA cm^{-2}), which proved that adding Ni metal salt in the synthesis process could improve the catalytic effect. LSV tests with diverse Fe and Co doping levels are further detailed in Figure S5, which proves that $\text{Co}_{0.45}\text{Fe}_{0.45}\text{Ni}_{0.9}\text{-MOF/NF}$ possesses superior performance (Figure S5) among these catalysts. In addition, the overpotentials of alkaline OER of $\text{Co}_{0.45}\text{Fe}_{0.45}\text{Ni}_{0.9}\text{-LDH/NF}$ and $\text{Co}_{0.45}\text{Fe}_{0.45}\text{Ni}_{0.9}\text{-MOF/NF}$ were compared. As shown in Figure S6, the overpotentials of $\text{Co}_{0.45}\text{Fe}_{0.45}\text{Ni}_{0.9}\text{-LDH/NF}$ at 50 mA cm^{-2} and 100 mA cm^{-2} were 280 mV and 313 mV, respectively, both of which were significantly higher than that of $\text{Co}_{0.45}\text{Fe}_{0.45}\text{Ni}_{0.9}\text{-MOF/NF}$, indicating that MOF has higher catalytic activity than that of LDH. The OER overpotential of $\text{Co}_{0.45}\text{Fe}_{0.45}\text{Ni}_{0.9}\text{-MOF/NF}$ under alkaline conditions compared to other catalysts is listed in Table S2, where it competes favorably, even against other top–tier catalysts.

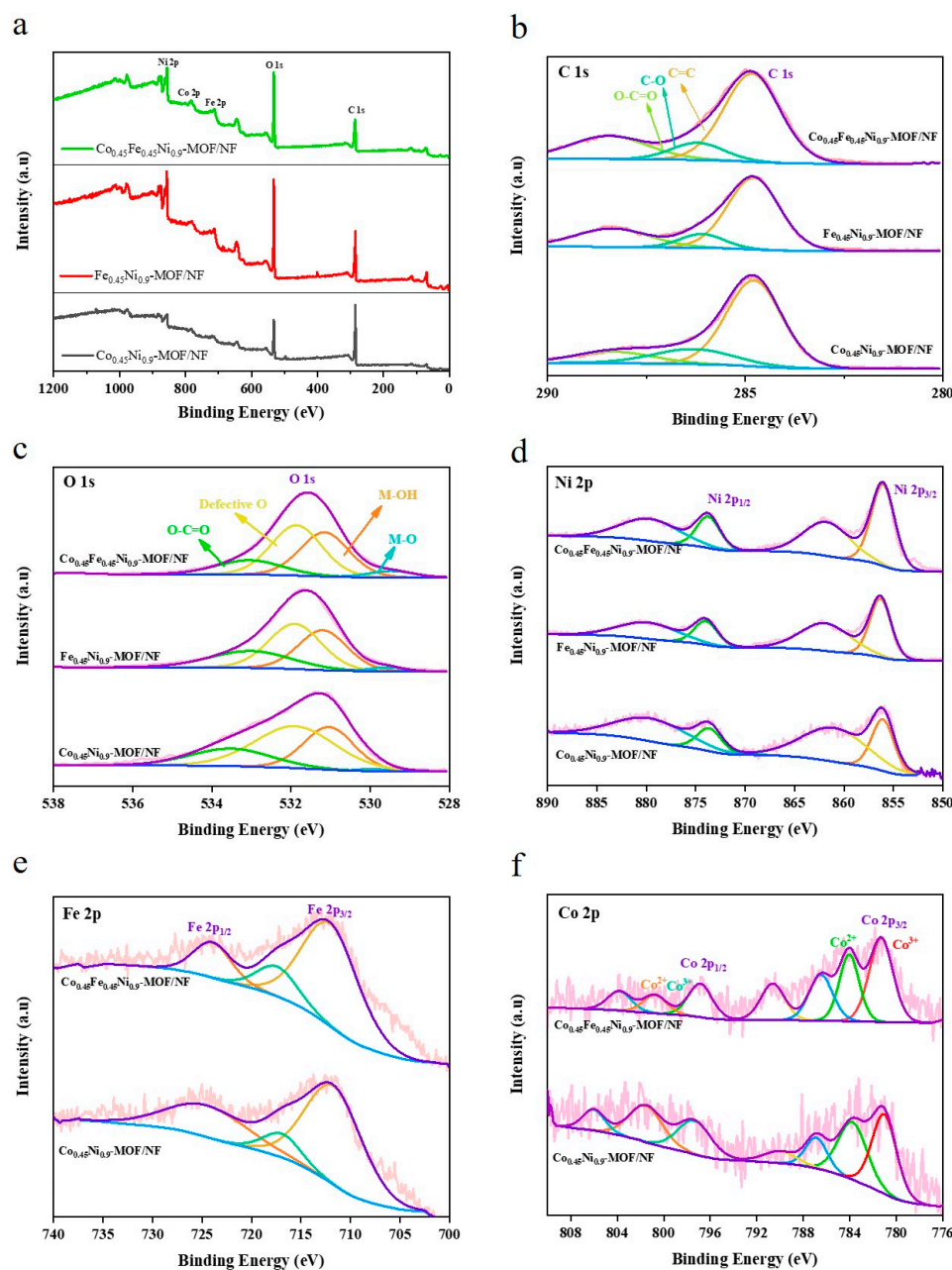


Figure 3. XPS spectra of $\text{Fe}_{0.45}\text{Ni}_{0.9}\text{-MOF/NF}$, $\text{Co}_{0.45}\text{Ni}_{0.9}\text{-MOF/NF}$, and $\text{Co}_{0.45}\text{Fe}_{0.45}\text{Ni}_{0.9}\text{-MOF/NF}$ for (a) full spectrum; (b) C 1s; (c) O 1s; (d) Ni 2p; (e) Fe 2p; and (f) Co 2p regions.

Figure 4b reveals that the Tafel slope of $\text{Co}_{0.45}\text{Fe}_{0.45}\text{Ni}_{0.9}\text{-MOF/NF}$ (127 mV dec^{-1}) is considerably lower than that of NF ($157.4 \text{ mV dec}^{-1}$), $\text{Fe}_{0.45}\text{Ni}_{0.9}\text{-MOF/NF}$ (140 mV dec^{-1}), and $\text{Co}_{0.45}\text{Ni}_{0.9}\text{-MOF/NF}$ ($151.5 \text{ mV dec}^{-1}$), suggesting an optimal reaction kinetics in CoFeNi-MOF/NF. Figure 4c shows the electrochemical impedance spectroscopy (EIS) readings for $\text{Co}_{0.45}\text{Fe}_{0.45}\text{Ni}_{0.9}\text{-MOF/NF}$, conducted at 1.5 V vs. RHE within the $10^5\text{-}0.01 \text{ Hz}$ frequency range, with insets of an impedance spectrum and an equivalent circuit diagram. It can be seen from Figure 4c that series resistance ($R_s = 1.686 \Omega$) and charge transfer impedance ($R_{ct} = 0.885 \Omega$) of $\text{Co}_{0.45}\text{Fe}_{0.45}\text{Ni}_{0.9}\text{-MOF/NF}$ are notably lower than those of other catalysts, suggesting enhanced electrical conductivity and rapid surface charge transfer [52].

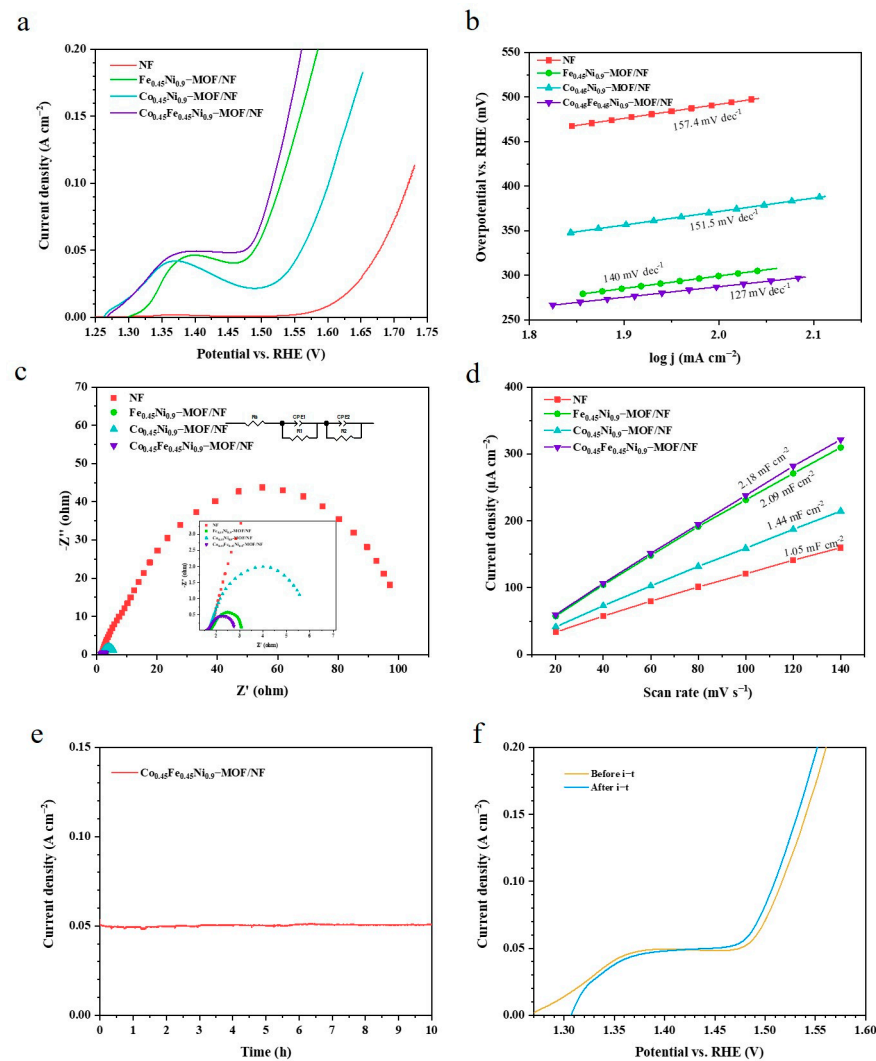


Figure 4. OER performance under 1 M KOH: (a) LSV curves; (b) Tafel plot; (c) Nyquist plot measured at 1.5 V vs. RHE and (d) C_{dl} measured at non-Faradaic region of NF, $\text{Fe}_{0.45}\text{Ni}_{0.9}\text{-MOF/NF}$, $\text{Co}_{0.45}\text{Ni}_{0.9}\text{-MOF/NF}$, and $\text{Co}_{0.45}\text{Fe}_{0.45}\text{Ni}_{0.9}\text{-MOF/NF}$; (e) $i\text{-}t$ test curve; and (f) LSV curve before and after $i\text{-}t$ test of $\text{Co}_{0.45}\text{Fe}_{0.45}\text{Ni}_{0.9}\text{-MOF/NF}$.

Given that a catalyst's electrochemically active surface area (ECSA) is directly proportional to its double-layer capacitance (C_{dl}), the ECSA can be estimated by measuring the C_{dl} of a sample [53,54]. Figure 4d shows that the C_{dl} of $\text{Co}_{0.45}\text{Fe}_{0.45}\text{Ni}_{0.9}\text{-MOF/NF}$ (2.18 mF cm^{-2}) surpasses those of $\text{Fe}_{0.45}\text{Ni}_{0.9}\text{-MOF/NF}$ (2.09 mF cm^{-2}), $\text{Co}_{0.45}\text{Ni}_{0.9}\text{-MOF/NF}$ (1.44 mF cm^{-2}), and NF (1.05 mF cm^{-2}). This signifies that $\text{Co}_{0.45}\text{Fe}_{0.45}\text{Ni}_{0.9}\text{-MOF/NF}$ offers a larger active surface area for water electrolysis within a fixed catalyst geometric area [8,55]. SEM morphology of $\text{Co}_{0.45}\text{Fe}_{0.45}\text{Ni}_{0.9}\text{-MOF/NF}$ in Figure 1a corroborates the hypothesis that the bowknot flake microstructure exhibits a larger specific surface area, thus making more active sites accessible. This, coupled with the ECSA-normalized LSV curves in Figure S7, highlights the exceptional site activity compared to other catalysts. Notably, the formula applied to calculate ECSA is $ECSA = \frac{C_s}{C_{dl}}$, with C_s derived from an established value of 0.05 mF cm^{-2} [8,18].

The stability of the electrocatalyst is one of the most important characteristics for practical application. In this work, the stability of the catalyst was estimated by recording the change in current density with time at constant potential (as shown in Figure 4e). After the 10 h stability test, the current density of $\text{Co}_{0.45}\text{Fe}_{0.45}\text{Ni}_{0.9}\text{-MOF/NF}$ did not change significantly compared to the initial current density of 50 mA cm^{-2} , indicating

excellent stability in OER. In addition, it can be seen from Figure 4f that the catalytical performance of $\text{Co}_{0.45}\text{Fe}_{0.45}\text{Ni}_{0.9}\text{-MOF/NF}$ had a slight improvement after the stability test, which might be attributed to the morphology change in the catalyst before and after the stability test. The SEM image in Figure S8a indicates an altered microstructure after the stability test. The morphology of the catalyst became sparser than that of before the test, and the needle-like and flaky structures coexist, potentially leading to enhanced exposure and activation of intrinsic active sites [18]. As shown in Figure S8b,c, EDS analysis was performed on the sample after OER *i-t* test under 1 M KOH. The results showed an increase in the percentage content of both Fe and Ni, which might be due to the change in morphology that allows the electron beam to hit deeper material. The content of C decreased, the content of O increased, and the LSV performance was better after the stability test, indicating that the real electrocatalytic active component in the material might be the metal hydroxide or oxyhydroxide generated by the electrochemical reconstruction of crystalline $\text{Co}_{0.45}\text{Fe}_{0.45}\text{Ni}_{0.9}\text{-MOF/NF}$ [46,56,57].

The electrochemical performance of the catalysts was estimated in 1 M phosphate-buffered saline (PBS) solution to discern their OER catalytic prowess under neutral conditions. The disparities among these catalysts with varied molar ratios of Fe and Co were estimated as shown in Figure S9. It can be seen that the overall current density for all samples remains subdued due to the limited ion concentration demanded by reaction intermediates; however, the $\text{Co}_{0.45}\text{Fe}_{0.45}\text{Ni}_{0.9}\text{-MOF/NF}$ emerges as the standout performer in this cohort.

It can be seen from Figure 5a that only 505 mV was required for $\text{Co}_{0.45}\text{Fe}_{0.45}\text{Ni}_{0.9}\text{-MOF/NF}$ to drive a current density of 10 mA cm^{-2} , which is much smaller than that of $\text{Fe}_{0.45}\text{Ni}_{0.9}\text{-MOF/NF}$ (625 mV) and $\text{Co}_{0.45}\text{Ni}_{0.9}\text{-MOF/NF}$ (565 mV). Benchmarking against other operational catalysts in Table S3, the OER performance of $\text{Co}_{0.45}\text{Fe}_{0.45}\text{Ni}_{0.9}\text{-MOF/NF}$ under neutral conditions remains commendable. Interestingly, under 1 M PBS condition, as opposed to the 1 M KOH setting, the OER performance of $\text{Co}_{0.45}\text{Ni}_{0.9}\text{-MOF/NF}$ outperforms that of $\text{Fe}_{0.45}\text{Ni}_{0.9}\text{-MOF/NF}$, emphasizing the enhancement of OER performance under neutral conditions when Co juxtaposes with Fe. This pronounced uplift in the OER performance of $\text{Co}_{0.45}\text{Fe}_{0.45}\text{Ni}_{0.9}\text{-MOF/NF}$ might be ascribed to the synergistic effect of Fe and Co with Ni, amplifying the inherent activity of the active sites [58].

Supportive evidence of superior OER reaction kinetics of $\text{Co}_{0.45}\text{Fe}_{0.45}\text{Ni}_{0.9}\text{-MOF/NF}$ under neutral conditions is further substantiated by the Tafel slope in Figure 5b and the EIS curve presented in Figure 5c. Besides its kinetic prowess, $\text{Co}_{0.45}\text{Fe}_{0.45}\text{Ni}_{0.9}\text{-MOF/NF}$ exhibits stellar stability during OER catalysis under neutral environments. Figure 5d,e highlight the near-identical current density of $\text{Co}_{0.45}\text{Fe}_{0.45}\text{Ni}_{0.9}\text{-MOF/NF}$ before and after a 10 h stability assessment. The congruence of LSV curves before and after the *i-t* test ratifies its electrochemical stability. However, the SEM image (as shown in Figure S10a) reveals that the bowknot flake morphology was changed to aggregated rod-like morphology, which might account for the marginal dip in performance, possibly due to diminished exposure of the active sites. EDS analysis was also performed on the sample after the OER *i-t* test under 1 M PBS as shown in Figure S10b,c. The proportions of Fe and Ni were almost consistent with the samples before the stability test, while the proportions of Co and O increased. It is speculated that, under neutral conditions, Co is the main active site in $\text{Co}_{0.45}\text{Fe}_{0.45}\text{Ni}_{0.9}\text{-MOF/NF}$, which is consistent with the test results in Figure 5a, and then, it is slowly converted into metal oxide in the *i-t* test [59].

To encapsulate, Figure 5f consolidates the OER overpotentials of 1 M KOH and 1 M PBS for each comparative material, unambiguously spotlighting the unmatched superiority of $\text{Co}_{0.45}\text{Fe}_{0.45}\text{Ni}_{0.9}\text{-MOF/NF}$ across diverse testing environments and current densities.

Encouraged by the remarkable OER performance of MOFs under both alkaline and neutral conditions, we assessed the HER catalytic capabilities of these catalysts under both environments, aiming to determine their suitability as bifunctional catalysts. Preliminary experimental results with different Co and Fe molar ratios are shown in Figure S11.

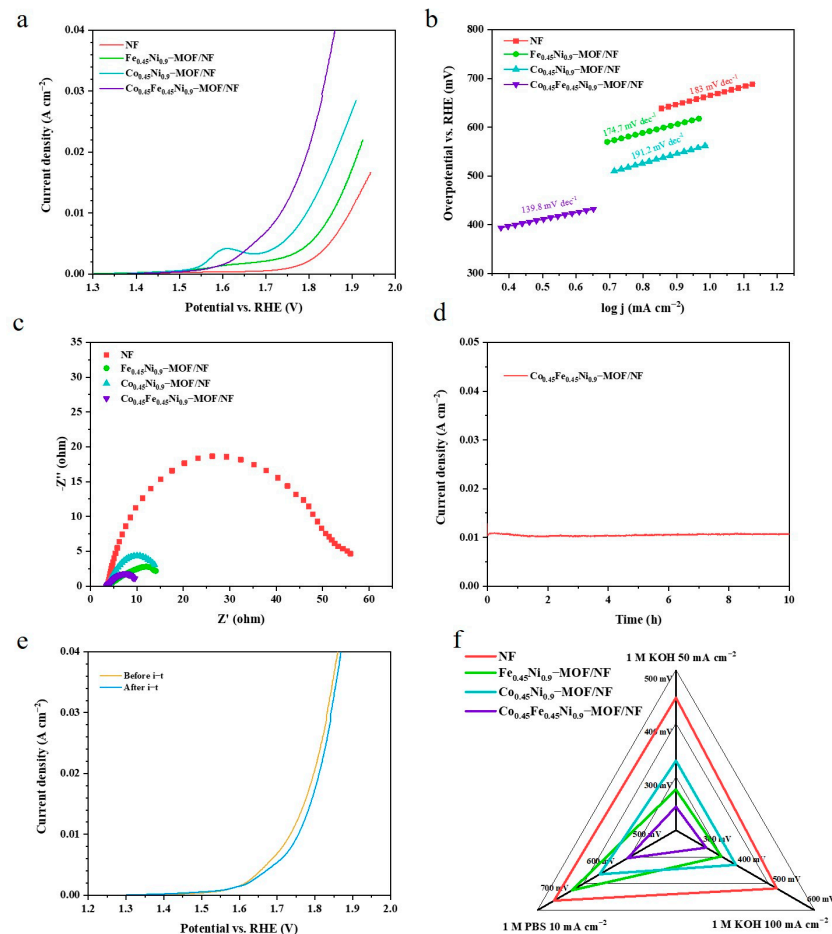


Figure 5. OER performance under 1 M PBS: (a) LSV curves; (b) Tafel plot; (c) Nyquist plot measured at 1.8 V vs. RHE of NF, Fe_{0.45}Ni_{0.9}-MOF/NF, Co_{0.45}Ni_{0.9}-MOF/NF, and Co_{0.45}Fe_{0.45}Ni_{0.9}-MOF/NF; (d) i-t test curve and (e) LSV curve before and after i-t of Co_{0.45}Fe_{0.45}Ni_{0.9}-MOF/NF; and (f) the comparison of overpotentials at 10 mA cm⁻² under 1 M PBS, 50 mA cm⁻² and 100 mA cm⁻² under 1 M KOH of NF, Fe_{0.45}Ni_{0.9}-MOF/NF, Co_{0.45}Ni_{0.9}-MOF/NF, and Co_{0.45}Fe_{0.45}Ni_{0.9}-MOF/NF.

Under 1 M KOH environment, Co_{0.45}Fe_{0.45}Ni_{0.9}-MOF/NF requires the lowest overpotential of 164 mV to achieve a current density of 10 mA cm⁻² among these catalysts, as shown in Figure 6a. Similarly, the HER performances of Co_{0.45}Fe_{0.45}Ni_{0.9}-LDH/NF and Co_{0.45}Fe_{0.45}Ni_{0.9}-MOF/NF under 1 M KOH were compared. As shown in Figure S12, LDH needs an overpotential of 225 mV to drive the current density of 10 mA cm⁻² in HER catalysis, which has a significant disparity with that of Co_{0.45}Fe_{0.45}Ni_{0.9}-MOF/NF, demonstrating once again the performance advantage of MOF in electrocatalysis. Moreover, the Co_{0.45}Fe_{0.45}Ni_{0.9}-MOF/NF with a Tafel slope of 91.6 mV dec⁻¹, Fe_{0.45}Ni_{0.9}-MOF/NF of 123.3 mV dec⁻¹, Co_{0.45}Ni_{0.9}-MOF/NF of 100.3 mV dec⁻¹, and NF of 134 mV dec⁻¹ shown in Figure 6b all conform to the Volmer–Heyrovsky rate-determining step [60,61]. Even though the HER stability of Co_{0.45}Fe_{0.45}Ni_{0.9}-MOF/NF is not as extraordinary as that of OER, it still shows commendable stability after the 10 h i-t test without a notable current density drop (as shown in Figure 6c). Figure 6d,e show the LSV curves and Tafel plots of HER under 1 M PBS environment. It can be seen from Figure 6d,e that Co_{0.45}Fe_{0.45}Ni_{0.9}-MOF/NF requires the lowest overpotential of 241 mV to drive a current density of 10 mA cm⁻² and exhibits a higher reaction kinetics rate. Tables S4 and S5 offer a comparative lens into the HER performance between Co_{0.45}Fe_{0.45}Ni_{0.9}-MOF/NF and other studies under alkaline and near-neutral conditions, respectively. Undoubtedly, Co_{0.45}Fe_{0.45}Ni_{0.9}-MOF/NF consistently outperforms its counterparts in HER under varying pH conditions, displaying unmatched kinetic advantages.

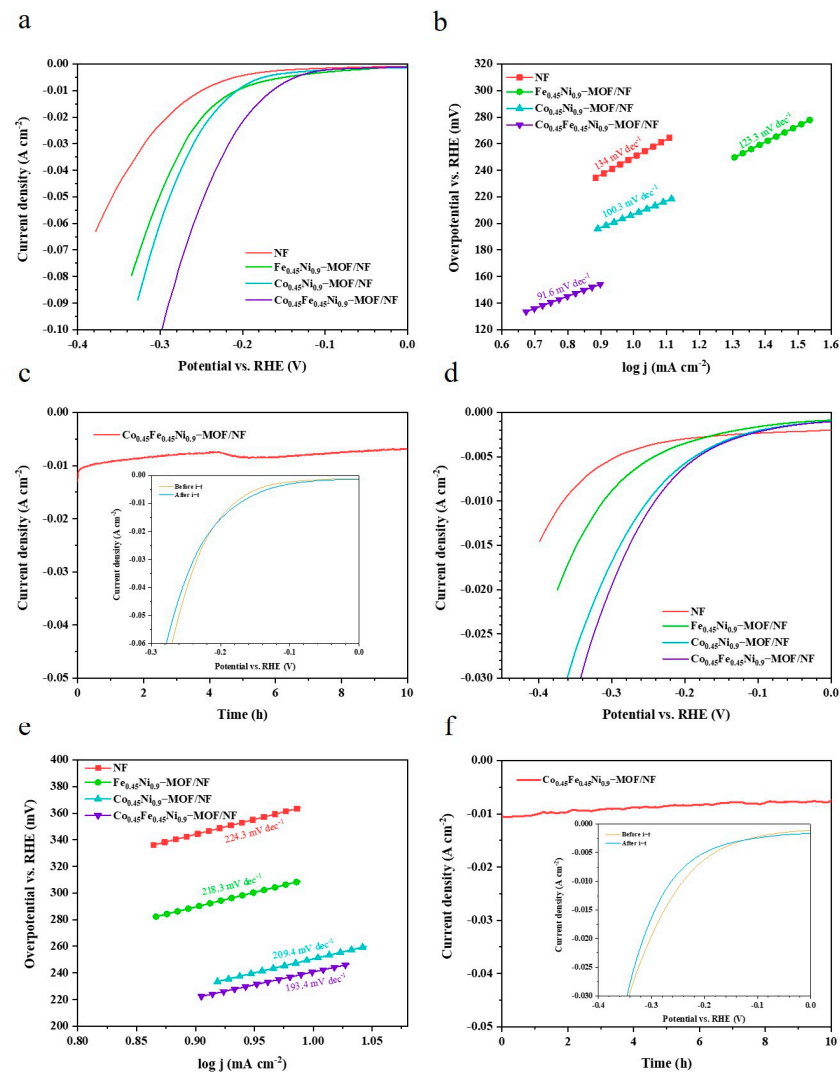


Figure 6. HER performance under 1 M KOH: (a) LSV curve; (b) Tafel plot of NF, $\text{Fe}_{0.45}\text{Ni}_{0.9}\text{-MOF/NF}$, $\text{Co}_{0.45}\text{Ni}_{0.9}\text{-MOF/NF}$, and $\text{Co}_{0.45}\text{Fe}_{0.45}\text{Ni}_{0.9}\text{-MOF/NF}$; and (c) i - t curve and the inset is the LSV curve before and after i - t test of $\text{Co}_{0.45}\text{Fe}_{0.45}\text{Ni}_{0.9}\text{-MOF/NF}$. HER performance under 1 M PBS: (d) LSV curve; (e) Tafel plot of NF, $\text{Fe}_{0.45}\text{Ni}_{0.9}\text{-MOF/NF}$, $\text{Co}_{0.45}\text{Ni}_{0.9}\text{-MOF/NF}$, and $\text{Co}_{0.45}\text{Fe}_{0.45}\text{Ni}_{0.9}\text{-MOF/NF}$; and (f) i - t curve and the inset plot is the LSV curve before and after i - t test of $\text{Co}_{0.45}\text{Fe}_{0.45}\text{Ni}_{0.9}\text{-MOF/NF}$.

Additionally, HER Nyquist plots across different environments in Figure S13 also reiterate that $\text{Co}_{0.45}\text{Fe}_{0.45}\text{Ni}_{0.9}\text{-MOF/NF}$ has minimal resistance and superior charge transfer rates. Stability testing results (Figure 6f) demonstrate the capability of $\text{Co}_{0.45}\text{Fe}_{0.45}\text{Ni}_{0.9}\text{-MOF/NF}$ to execute HER performances under neutral environments with unwavering consistency. The SEM images of the catalysts after the HER tests under both 1 M KOH and 1 M PBS are shown in Figure S14, respectively, where the morphology of the aggregate block conceals the active site, and this might explain the marginal performance decline. Collectively, this evidence proves that $\text{Co}_{0.45}\text{Fe}_{0.45}\text{Ni}_{0.9}\text{-MOF/NF}$ might serve as a versatile bifunctional catalyst, excelling in both OER and HER under alkaline and neutral environments.

The accumulated experimental evidence unequivocally demonstrates the superior catalytic prowess of $\text{Co}_{0.45}\text{Fe}_{0.45}\text{Ni}_{0.9}\text{-MOF/NF}$ in both OER and HER processes, spanning alkaline and neutral environments. Motivated by these findings, we proceeded to assemble an overall water splitting cell, designating $\text{Co}_{0.45}\text{Fe}_{0.45}\text{Ni}_{0.9}\text{-MOF/NF}$ as both the anode and cathode, which was conducted via a two-electrode system.

As shown in Figure 7a, the LSV curve resulting from the $\text{Co}_{0.45}\text{Fe}_{0.45}\text{Ni}_{0.9}\text{-MOF/NF} \parallel \text{Co}_{0.45}\text{Fe}_{0.45}\text{Ni}_{0.9}\text{-MOF/NF}$ configuration for overall water splitting highlights an impressive efficiency under alkaline conditions. A small working voltage of 1.59 V is sufficient to drive a current density of 10 mA cm^{-2} . When compared to a slew of competing catalysts, the performance of this catalyst is prominently elite, as evident from Table S6. Furthermore, this dual-functional electrocatalyst exhibited exceptional durability. It was found that there was no observable performance decline compared to the initial LSV after consistently operating at a current density of 10 mA cm^{-2} over a spanning time of 10 h.

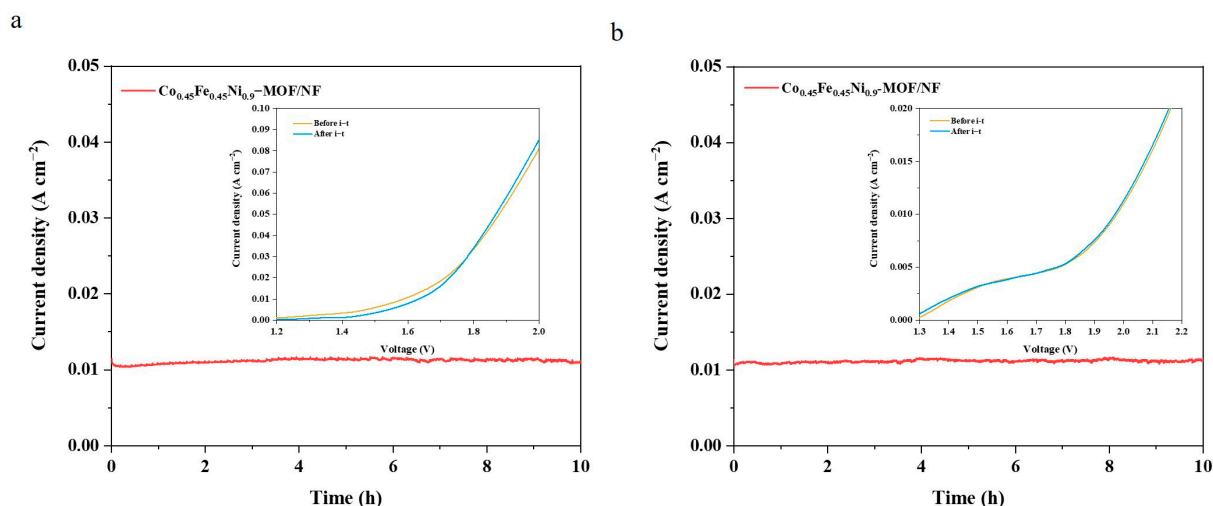


Figure 7. Overall water splitting performance of $\text{Co}_{0.45}\text{Fe}_{0.45}\text{Ni}_{0.9}\text{-MOF/NF} \parallel \text{Co}_{0.45}\text{Fe}_{0.45}\text{Ni}_{0.9}\text{-MOF/NF}$: (a) durability test in 1 M KOH and the inset is the LSV curve before and after *i-t* test and (b) durability test in 1 M PBS and the inset is the LSV curve before and after *i-t* test.

Our exploration continued by employing the catalyst as both an anode and a cathode in a 1 M PBS system, as illustrated in Figure 7b. Although the potential needed to achieve a current density of 10 mA cm^{-2} is elevated to 1.97 V compared to its alkaline counterpart, the catalyst still displayed commendable stability over a 10 h span. The LSV curves, before and after the durability tests, remained strikingly congruent, further bolstering its credentials as a versatile dual-function catalyst for neutral water electrolysis.

4. Conclusions

In the pursuit of a sustainable and environmentally friendly synthesis strategy of electrocatalyst for water splitting, this work successfully prepared a catalyst of $\text{Co}_{0.45}\text{Fe}_{0.45}\text{Ni}_{0.9}\text{-MOF/NF}$ via the shape-preserving two-step hydrothermal method. A distinctive bowknot flake-like structure was successfully obtained on NF, which increased the electrocatalytic surface area significantly, leading to a pronounced increase in the effective electrocatalytic active sites. Our comprehensive investigations highlighted the exceptional performances of this catalyst in oxygen evolution reaction (OER) and hydrogen evolution reaction (HER) under both alkaline and neutral conditions. The strategic synergy of Co and Fe within this framework not only improved the intrinsic activity at the catalytic sites but also accelerated the electron transfer. These combined attributes make a catalyst to exhibit commendable current densities, minimized overpotentials, and rapid charge transfer dynamics, setting it apart in terms of efficiency and stability. Furthermore, the $\text{Co}_{0.45}\text{Fe}_{0.45}\text{Ni}_{0.9}\text{-MOF/NF}$ catalyst exhibits superior properties as a bifunctional catalyst in overall water splitting, a pivotal step towards holistic renewable energy solutions. The innovative shape-preserving synthesis method introduced in this research sets a benchmark, offering valuable insights and a robust foundation for future endeavors in the realm of advanced electrocatalysts for water splitting.

Supplementary Materials: The following are available online at <https://www.mdpi.com/article/10.3390/ma17102195/s1>, Figure S1: SEM images of (a) $\text{Co}_{0.45}\text{Fe}_{0.45}\text{Ni}_{0.9}\text{-LDH/NF}$ and (b) $\text{Co}_{0.45}\text{Fe}_{0.45}\text{Ni}_{0.9}\text{-MOF/NF}$, Figure S2. SEM images of (a) $\text{Fe}_{0.45}\text{Ni}_{0.9}\text{-MOF/NF}$; (b) $\text{Co}_{0.9}\text{Fe}_{0.45}\text{Ni}_{0.9}\text{-MOF/NF}$; (c) $\text{Co}_{0.45}\text{Ni}_{0.9}\text{-MOF/NF}$; and (d) $\text{Co}_{0.45}\text{Fe}_{0.9}\text{Ni}_{0.9}\text{-MOF/NF}$, Figure S3. EDS spectrum of $\text{Co}_{0.45}\text{Fe}_{0.45}\text{Ni}_{0.9}\text{-MOF/NF}$, Figure S4. (a,b) HRTEM images and (c–f) EDS elemental mapping of $\text{Co}_{0.45}\text{Fe}_{0.45}\text{Ni}_{0.9}\text{-MOF/NF}$, Figure S5. LSV curves of OER under 1 M KOH for the catalysts with different dosages of (a) Co and (b) Fe., Figure S6. LSV curves of OER under 1 M KOH for $\text{Co}_{0.45}\text{Fe}_{0.45}\text{Ni}_{0.9}\text{-LDH/NF}$ and $\text{Co}_{0.45}\text{Fe}_{0.45}\text{Ni}_{0.9}\text{-MOF/NF}$, Figure S7. ECSA-normalized LSV curves of NF, $\text{Fe}_{0.45}\text{Ni}_{0.9}\text{-MOF/NF}$, $\text{Co}_{0.45}\text{Ni}_{0.9}\text{-MOF/NF}$, and $\text{Co}_{0.45}\text{Fe}_{0.45}\text{Ni}_{0.9}\text{-MOF/NF}$, Figure S8. (a–b) SEM images of $\text{Co}_{0.45}\text{Fe}_{0.45}\text{Ni}_{0.9}\text{-MOF/NF}$ after OER i-t test under 1 M KOH with different magnifications and (c) EDS spectrum of (b), Figure S9. OER LSV curves under 1 M PBS for different dosages of (a) Co and (b) Fe., Figure S10. (a–b) SEM images of $\text{Co}_{0.45}\text{Fe}_{0.45}\text{Ni}_{0.9}\text{-MOF/NF}$ after OER i-t test under 1 M PBS with different magnifications and (c) EDS spectrum of (b), Figure S11. HER LSV curves under 1 M KOH with different dosages of (a) Co and (b) Fe. HER LSV curves at 1 M PBS with different dosages of (c) Co and (d) Fe., Figure S12. LSV curves of HER under 1 M KOH for $\text{Co}_{0.45}\text{Fe}_{0.45}\text{Ni}_{0.9}\text{-LDH/NF}$ and $\text{Co}_{0.45}\text{Fe}_{0.45}\text{Ni}_{0.9}\text{-MOF/NF}$, Figure S13. Nyquist plots measured at -0.3 V vs. RHE of NF, $\text{Fe}_{0.45}\text{Ni}_{0.9}\text{-MOF/NF}$, $\text{Co}_{0.45}\text{Ni}_{0.9}\text{-MOF/NF}$, and $\text{Co}_{0.45}\text{Fe}_{0.45}\text{Ni}_{0.9}\text{-MOF/NF}$ under (a) 1 M KOH and (b) 1 M PBS, respectively, Figure S14. SEM images of $\text{Co}_{0.45}\text{Fe}_{0.45}\text{Ni}_{0.9}\text{-MOF/NF}$ after the i-t test of HER under (a) 1 M KOH and (b) 1 M PBS, respectively, Table S1: ICP-OES test of metallic elements in $\text{Co}_{0.45}\text{Fe}_{0.45}\text{Ni}_{0.9}\text{-MOF/NF}$, Table S2. Comparison of OER performance for $\text{Co}_{0.45}\text{Fe}_{0.45}\text{Ni}_{0.9}\text{-MOF/NF}$ with other non-noble-metal-based catalysts under alkaline conditions., Table S3. Comparison of OER performance for $\text{Co}_{0.45}\text{Fe}_{0.45}\text{Ni}_{0.9}\text{-MOF/NF}$ with other non-noble-metal-based catalysts under near-neutral conditions., Table S4. Comparison of HER performance for $\text{Co}_{0.45}\text{Fe}_{0.45}\text{Ni}_{0.9}\text{-MOF/NF}$ with other non-noble-metal-based catalysts under alkaline conditions., Table S5. Comparison of HER performance for $\text{Co}_{0.45}\text{Fe}_{0.45}\text{Ni}_{0.9}\text{-MOF/NF}$ with other non-noble-metal-based catalysts under near-neutral conditions., Table S6. Comparison of overall water splitting performance for $\text{Co}_{0.45}\text{Fe}_{0.45}\text{Ni}_{0.9}\text{-MOF/NF}$ with other non-noble-metal-based catalysts under alkaline conditions. References [62–104] are cited in Supplementary Materials.

Author Contributions: Conceptualization and Methodology, L.G.; Investigation, Y.L.; Writing—original draft, Y.L.; Writing—review & editing, P.L., Z.W. and L.G.; Supervision, L.G.; Funding acquisition, L.G. All authors have read and agreed to the published version of the manuscript.

Funding: This work was supported by the Fundamental Research Funds for the Central Universities, Sichuan University (YJ2021166), and the Natural Science Foundation of Sichuan Province (2024NSFSC1450).

Institutional Review Board Statement: Not applicable.

Informed Consent Statement: Not applicable.

Data Availability Statement: The data supporting the article’s findings are available from the corresponding author upon reasonable request.

Acknowledgments: Special thanks to Yue Qi for the XRD measurements at the comprehensive training platform of the Specialized Laboratory in the College of Chemistry, Sichuan University. Special thanks to Xiaoshan Zhang for the SEM measurements at the College of Materials Science and Engineering, Sichuan University. In addition, we are also grateful for the SEM and XPS characterizations provided by “shiyanjia lab” (www.shiyanjia.com (accessed on 20 April 2024)).

Conflicts of Interest: The authors declare no conflict of interest.

References

1. Rajagopal, K.; Kathiresan, M.; Rajaram, A.; Natarajan, A.; Natesan, K. Development of robust noble-metal free lanthanum, neodymium doped $\text{Li}_{1.05}\text{Ni}_{0.5}\text{Mn}_{1.5}\text{O}_4$ as a bifunctional electrocatalyst for electrochemical water splitting. *RSC Adv.* **2023**, *13*, 23829–23840. [[CrossRef](#)] [[PubMed](#)]
2. Sai, K.N.S.; Tang, Y.; Dong, L.; Yu, X.Y.; Hong, Z. N_2 plasma-activated NiO nanosheet arrays with enhanced water splitting performance. *Nanotechnology* **2020**, *31*, 455709. [[CrossRef](#)]

3. Santhosh Kumar, R.; Ramakrishnan, S.; Prabhakaran, S.; Kim, A.R.; Kumar, D.R.; Kim, D.H.; Yoo, D.J. Structural, electronic, and electrocatalytic evaluation of spinel transition metal sulfide supported reduced graphene oxide. *J. Mater. Chem. A* **2022**, *10*, 1999–2011. [[CrossRef](#)]
4. Tee, S.Y.; Win, K.Y.; Teo, W.S.; Koh, L.D.; Liu, S.; Teng, C.P.; Han, M.Y. Recent Progress in Energy-Driven Water Splitting. *Adv. Sci.* **2017**, *4*, 37438–37475. [[CrossRef](#)]
5. Gao, T.; Yu, S.; Chen, Y.; Li, X.; Tang, X.; Wu, S.; He, B.; Lan, H.; Li, S.; Yue, Q.; et al. Regulating the thickness of the carbon coating layer in iron/carbon heterostructures to enhance the catalytic performance for oxygen evolution reaction. *J. Colloid. Interface Sci.* **2023**, *642*, 120–128. [[CrossRef](#)] [[PubMed](#)]
6. Seufferling, T.E.; Larson, T.R.; Barforoush, J.M.; Leonard, K.C. Carbonate-Derived Multi-Metal Catalysts for Electrochemical Water-Splitting at High Current Densities. *ACS Sustain. Chem. Eng.* **2021**, *9*, 16678–16686. [[CrossRef](#)]
7. Niyitanga, T.; Jeong, H.K. Hydrogen and oxygen evolution reactions of molybdenum disulfide synthesized by hydrothermal and plasma method. *J. Electroanal. Chem.* **2019**, *849*, 113383. [[CrossRef](#)]
8. McCrory, C.C.L.; Jung, S.; Peters, J.C.; Jaramillo, T.F. Benchmarking Heterogeneous Electrocatalysts for the Oxygen Evolution Reaction. *J. Am. Chem. Soc.* **2013**, *135*, 16977–16987. [[CrossRef](#)]
9. Gao, T.; Tang, X.; Li, X.; Lan, H.; Yu, S.; Wu, S.; Yue, Q.; Xiao, D. Surface reconstructing hierarchical structures as robust sulfion oxidation catalysts to produce hydrogen with ultralow energy consumption. *Inorg. Chem. Front.* **2023**, *10*, 1447–1456. [[CrossRef](#)]
10. Das, D.; Santra, S.; Nanda, K.K. In Situ Fabrication of a Nickel/Molybdenum Carbide-Anchored N-Doped Graphene/CNT Hybrid: An Efficient (Pre)catalyst for OER and HER. *ACS Appl. Mater. Interfaces* **2018**, *10*, 35025–35038. [[CrossRef](#)]
11. Zubaid, S.; Khan, J.; Sherazi, T.A. The influence of nanostructure and electrolyte concentration on the performance of nickel sulfide (Ni₃S₂) catalyst for electrochemical overall water splitting. *J. Colloid. Interface Sci.* **2024**, *660*, 502–512. [[CrossRef](#)] [[PubMed](#)]
12. Munawar, T.; Bashir, A.; Batoo, K.M.; Mukhtar, F.; Nadeem, M.S.; Hussain, S.; Manzoor, S.; Ashiq, M.N.; Khan, S.A.; Koc, M.; et al. Efficient rGO-supported CeO₂-Y₂O₃-Nd₂O₃ nanocomposite electrocatalyst for water splitting (HER/OER) in alkaline medium. *J. Korean Ceram. Soc.* **2024**, *15*. [[CrossRef](#)]
13. Jamesh, M.-I.; Harb, M. Tuning the electronic structure of the earth-abundant electrocatalysts for oxygen evolution reaction (OER) to achieve efficient alkaline water splitting—A review. *J. Energy Chem.* **2021**, *56*, 299–342. [[CrossRef](#)]
14. Sardar, K.; Petrucco, E.; Hiley, C.I.; Sharman, J.D.B.; Wells, P.P.; Russell, A.E.; Kashtiban, R.J.; Sloan, J.; Walton, R.I. Water-Splitting Electrocatalysis in Acid Conditions Using Ruthenate-Iridate Pyrochlores. *Angew. Chem. Int. Ed.* **2014**, *53*, 10960–10964. [[CrossRef](#)] [[PubMed](#)]
15. Tan, D.; Xiong, H.; Zhang, T.; Fan, X.; Wang, J.; Xu, F. Recent progress in noble-metal-free electrocatalysts for alkaline oxygen evolution reaction. *Front. Chem.* **2022**, *10*, 1071274. [[CrossRef](#)] [[PubMed](#)]
16. Kim, B.; Kim, T.; Lee, K.; Li, J. Recent Advances in Transition Metal Phosphide Electrocatalysts for Water Splitting under Neutral pH Conditions. *ChemElectroChem* **2020**, *7*, 3578–3589. [[CrossRef](#)]
17. Anantharaj, S.; Aravindan, V. Developments and Perspectives in 3d Transition-Metal-Based Electrocatalysts for Neutral and Near-Neutral Water Electrolysis. *Adv. Energy Mater.* **2019**, *10*, 1902666. [[CrossRef](#)]
18. Jothi, M.; Gnanasekar, P.; Kulandaivel, J. NiCo-Metal Organic Frameworks for Highly Stable Electrocatalytic Water Splitting under Alkaline and Neutral pH Ranges. *Energy Fuels* **2022**, *36*, 13713–13721. [[CrossRef](#)]
19. Subramaniam, M.R.; Ramakrishnan, S.; Sidra, S.; Karthikeyan, S.C.; Vijayapradeep, S.; Huang, J.; Mamlouk, M.; Kim, D.H.; Yoo, D.J. Carbon core-shell Pt nanoparticle embedded porphyrin Co-MOF derived N-doped porous carbon for the alkaline AEM water electrolyzer application. *J. Mater. Chem. A* **2024**, *12*, 5967–5979. [[CrossRef](#)]
20. Dey, G.; Shadab; Aijaz, A. Metal-Organic Framework Derived Nanostructured Bifunctional Electrocatalysts for Water Splitting. *ChemElectroChem* **2021**, *8*, 3782–3803. [[CrossRef](#)]
21. Ma, Y.; Miao, Y.; Mu, G.; Lin, D.; Xu, C.; Zeng, W.; Xie, F. Highly Enhanced OER Performance by Er-Doped Fe-MOF Nanoarray at Large Current Densities. *Nanomaterials* **2021**, *11*, 1847. [[CrossRef](#)]
22. Park, K.; Kwon, J.; Jo, S.; Choi, S.; Enkhtuvshin, E.; Kim, C.; Lee, D.; Kim, J.; Sun, S.; Han, H.; et al. Simultaneous electrical and defect engineering of nickel iron metal-organic-framework via co-doping of metalloid and non-metal elements for a highly efficient oxygen evolution reaction. *Chem. Eng. J.* **2022**, *439*, 135720. [[CrossRef](#)]
23. Gu, J.; He, J.; Zheng, H.; Sun, C. Morphology control in the synthesis of [Mo₃S₁₃]²⁻/Co-MOF-74 composite catalysts and their application in the oxygen evolution reaction. *New J. Chem.* **2023**, *47*, 8507–8514. [[CrossRef](#)]
24. Jiao, L.; Zhou, Y.X.; Jiang, H.L. Metal-organic framework-based CoP/reduced graphene oxide: High-performance bifunctional electrocatalyst for overall water splitting. *Chem. Sci.* **2016**, *7*, 1690–1695. [[CrossRef](#)]
25. Wang, K.; Kang, J.; Jin, L.; Yang, L.; Liu, Y.; Li, Y.; Chen, G.; Xu, H. Defect engineering of MOF toward enhanced electrocatalytic water oxidation. *Ionics* **2023**, *29*, 5397–5403. [[CrossRef](#)]
26. Ehsan, M.A.; Khan, A.; Hakeem, A.S. Binary CoNi and Ternary FeCoNi Alloy Thin Films as High-Performance and Stable Electrocatalysts for Oxygen Evolution Reaction. *ACS Appl. Energy Mater.* **2023**, *6*, 9556–9567. [[CrossRef](#)]
27. Tang, L.; Cai, M.; Zhang, M.; Chen, X.; Cai, Z. LDH-assisted growth of FeCo bimetal-MOF nanorods for electrocatalytic oxygen evolution. *RSC Adv.* **2022**, *12*, 25112–25117. [[CrossRef](#)] [[PubMed](#)]
28. Cheng, W.; Wu, Z.P.; Luan, D.; Zang, S.Q.; Lou, X.W.D. Synergetic Cobalt-Copper-Based Bimetal-Organic Framework Nanoboxes toward Efficient Electrochemical Oxygen Evolution. *Angew. Chem. Int. Ed. Engl.* **2021**, *60*, 26397–26402. [[CrossRef](#)] [[PubMed](#)]

29. Tan, J.-B.; Wu, J.-Q.; Zhao, J.-W.; Xie, L.-J.; Li, G.-R. Highly dispersed ultrafine Ni particles embedded into MOF-74 arrays by partial carbonization for highly efficient hydrogen evolution. *Mater. Adv.* **2020**, *1*, 1212–1219. [[CrossRef](#)]
30. Zhang, D.; Huang, R.; Xie, H.; Li, R.; Liu, X.; Pan, M.; Lei, Y. Effect of the valence state of initial iron source on oxygen evolution activity of Fe-doped Ni-MOF. *Chem. Pap.* **2020**, *74*, 2775–2784. [[CrossRef](#)]
31. Ravipati, M.; Durai, L.; Badhulika, S. Single-Pot Solvothermal Synthesis of Single-Crystalline Nickel-Metal Organic Framework Nanosheets for Direct Iron Fuel Cell Applications. *ACS Appl. Energy Mater.* **2023**, *6*, 6901–6909. [[CrossRef](#)]
32. Sun, T.; Lin, S.; Xu, Z.; Li, L. In situ growth of an Fe-doped NiCo-MOF electrocatalyst from layered double hydroxide effectively enhances electrocatalytic oxygen evolution performance. *CrystEngComm* **2021**, *23*, 7650–7657. [[CrossRef](#)]
33. Vanaraj, R.; Vinodh, R.; Periyasamy, T.; Madhappan, S.; Babu, C.M.; Asrafali, S.P.; Haldhar, R.; Jayprakash Raorane, C.; Hwang, H.; Kim, H.-J.; et al. Capacitance Enhancement of Metal-Organic Framework (MOF) Materials by Their Morphology and Structural Formation. *Energy Fuels* **2022**, *36*, 4978–4991. [[CrossRef](#)]
34. Sarawade, P.; Tan, H.; Polshettiwar, V. Shape- and Morphology-Controlled Sustainable Synthesis of Cu, Co, and In Metal Organic Frameworks with High CO₂ Capture Capacity. *ACS Sustain. Chem. Eng.* **2012**, *1*, 66–74. [[CrossRef](#)]
35. Deng, T.; Lu, Y.; Zhang, W.; Sui, M.; Shi, X.; Wang, D.; Zheng, W. Inverted Design for High-Performance Supercapacitor Via Co(OH)₂-Derived Highly Oriented MOF Electrodes. *Adv. Energy Mater.* **2017**, *8*, 1702294. [[CrossRef](#)]
36. Li, L.; Wang, Z.; She, X.; Pan, L.; Xi, C.; Wang, D.; Yi, J.; Yang, J. Ni-modified FeOOH integrated electrode by self-source corrosion of nickel foam for high-efficiency electrochemical water oxidation. *J. Colloid. Interface Sci.* **2023**, *652*, 789–797. [[CrossRef](#)] [[PubMed](#)]
37. Liu, Q.; Xie, L.; Liu, Z.; Du, G.; Asiri, A.M.; Sun, X. A Zn-doped Ni₃S₂ nanosheet array as a high-performance electrochemical water oxidation catalyst in alkaline solution. *Chem. Commun.* **2017**, *53*, 12446–12449. [[CrossRef](#)] [[PubMed](#)]
38. Cheng, R.; Zhan, C.; Gao, J. The direct growth of Mn_{0.6}Ni_{0.4}CO₃ nanosheet assemblies on Ni foam for high-performance supercapacitor electrodes. *New J. Chem.* **2022**, *46*, 2635–2640. [[CrossRef](#)]
39. Constantino, V.R.L.; Pinnavaia, T.J. Basic Properties of Mg^{2+1-x}Al^{3+x} Layered Double Hydroxides Intercalated by Carbonate, Hydroxide, Chloride, and Sulfate Anions. *Inorg. Chem.* **1995**, *34*, 883–892. [[CrossRef](#)]
40. Lin, Y.; Wang, H.; Peng, C.K.; Bu, L.; Chiang, C.L.; Tian, K.; Zhao, Y.; Zhao, J.; Lin, Y.G.; Lee, J.M.; et al. Co-Induced Electronic Optimization of Hierarchical NiFe LDH for Oxygen Evolution. *Small* **2020**, *16*, e2002426. [[CrossRef](#)]
41. Guo, H.; Lu, X.; He, J.; Zhang, H.; Zhang, H.; Dong, Y.; Zhou, D.; Xia, Q. Co-MOF nanosheet supported on ZSM-5 with an improved catalytic activity for air epoxidation of olefins. *Mater. Chem. Phys.* **2023**, *294*, 127001. [[CrossRef](#)]
42. Dai, M.; Wang, J.; Li, L.; Wang, Q.; Liu, M.; Zhang, Y. High-performance Oxygen Evolution Catalyst Enabled by Interfacial Effect between CeO₂ and FeNi Metal-organic Framework. *Acta Chim. Sin.* **2020**, *78*, 355–362. [[CrossRef](#)]
43. Zhao, Y.; Du, Q.; Cao, X.; Chi, B.; Zhang, J.; Zhang, C.; Liu, T.; Wang, X.; Su, Y. Electronic structure and electrocatalytic activity of cerium-doped tantalum oxide. *J. Electroanal. Chem.* **2012**, *681*, 139–143. [[CrossRef](#)]
44. Wiktor, C.; Turner, S.; Zacher, D.; Fischer, R.A.; Tendeloo, G.V. Imaging of intact MOF-5 nanocrystals by advanced TEM at liquid nitrogen temperature. *Microporous Mesoporous Mater.* **2012**, *162*, 131–135. [[CrossRef](#)]
45. Gong, X.; Gnanasekaran, K.; Chen, Z.; Robison, L.; Wasson, M.C.; Bentz, K.C.; Cohen, S.M.; Farha, O.K.; Gianneschi, N.C. Insights into the Structure and Dynamics of Metal-Organic Frameworks via Transmission Electron Microscopy. *J. Am. Chem. Soc.* **2020**, *142*, 17224–17235. [[CrossRef](#)]
46. Yang, L.; Zhu, G.; Wen, H.; Guan, X.; Sun, X.; Feng, H.; Tian, W.; Zheng, D.; Cheng, X.; Yao, Y. Constructing a highly oriented layered MOF nanoarray from a layered double hydroxide for efficient and long-lasting alkaline water oxidation electrocatalysis. *J. Mater. Chem. A* **2019**, *7*, 8771–8776. [[CrossRef](#)]
47. Li, Z.; Xing, X.; Chu, J.; Wang, K.-L.; Yu, C.; Wei, Z.; Wen, Y.; Sun, H.; Wang, Z.-K. MOF confined in macroporous-mesoporous-TiO₂ for light-boosting electrocatalytic oxygen production. *Mater. Today Energy* **2019**, *13*, 125–133. [[CrossRef](#)]
48. Ni, S.; Qu, H.; Xu, Z.; Zhu, X.; Chen, L.; Xing, H.; Wu, X.; Liu, H.; Yang, L. Regulating the Spin State of Metal and Metal Carbide Heterojunctions for Efficient Oxygen Evolution. *ACS Appl. Mater. Interfaces* **2023**, *15*, 36423–36433. [[CrossRef](#)] [[PubMed](#)]
49. Zhang, X.; Fang, X.; Zhu, K.; Yuan, W.; Jiang, T.; Xue, H.; Tian, J. Fe-doping induced electronic structure reconstruction in Ni-based metal-organic framework for improved energy-saving hydrogen production via urea degradation. *J. Power Sources* **2022**, *520*, 230882. [[CrossRef](#)]
50. Hu, Z.; Hao, L.; Quan, F.; Guo, R. Recent developments of Co₃O₄-based materials as catalysts for the oxygen evolution reaction. *Catal. Sci. Technol.* **2022**, *12*, 436–461. [[CrossRef](#)]
51. Hu, Y.; Luo, G.; Wang, L.; Liu, X.; Qu, Y.; Zhou, Y.; Zhou, F.; Li, Z.; Li, Y.; Yao, T.; et al. Single Ru Atoms Stabilized by Hybrid Amorphous/Crystalline FeCoNi Layered Double Hydroxide for Ultraefficient Oxygen Evolution. *Adv. Energy Mater.* **2020**, *11*, 2002816. [[CrossRef](#)]
52. Ghadge, S.D.; Velikokhatnyi, O.I.; Datta, M.K.; Damodaran, K.; Shanthi, P.M.; Kumta, P.N. Highly Efficient Fluorine Doped Ni₂P Electrocatalysts for Alkaline Mediated Oxygen Evolution Reaction. *J. Electrochem. Soc.* **2021**, *168*, 064512. [[CrossRef](#)]
53. Karmakar, A.; Kundu, S. A concise perspective on the effect of interpreting the double layer capacitance data over the intrinsic evaluation parameters in oxygen evolution reaction. *Mater. Today Energy* **2023**, *33*, 101259. [[CrossRef](#)]
54. Jeon, S.S.; Kang, P.W.; Klingenhof, M.; Lee, H.; Dionigi, F.; Strasser, P. Active Surface Area and Intrinsic Catalytic Oxygen Evolution Reactivity of NiFe LDH at Reactive Electrode Potentials Using Capacitances. *ACS Catal.* **2023**, *13*, 1186–1196. [[CrossRef](#)]
55. Benck, J.D.; Chen, Z.; Kuritzky, L.Y.; Forman, A.J.; Jaramillo, T.F. Amorphous Molybdenum Sulfide Catalysts for Electrochemical Hydrogen Production: Insights into the Origin of their Catalytic Activity. *ACS Catal.* **2012**, *2*, 1916–1923. [[CrossRef](#)]

56. Muthukumar, P.; Arunkumar, G.; Pannipara, M.; Al-Sehemi, A.G.; Moon, D.; Anthony, S.P. Enhancing the electrocatalytic OER activity of Co-MOFs through labile solvents coordination. *New J. Chem.* **2023**, *47*, 20831–20837. [[CrossRef](#)]
57. Joshi, A.; Gaur, A.; Sood, P.; Singh, M. One-Pot Crystallization of 2D and 3D Cobalt-Based Metal–Organic Frameworks and Their High-Performance Electrocatalytic Oxygen Evolution. *Inorg. Chem.* **2021**, *60*, 12685–12690. [[CrossRef](#)] [[PubMed](#)]
58. Khalid, M.; Honorato, A.M.B.; Tremiliosi Filho, G.; Varela, H. Trifunctional catalytic activities of trimetallic FeCoNi alloy nanoparticles embedded in a carbon shell for efficient overall water splitting. *J. Mater. Chem. A* **2020**, *8*, 9021–9031. [[CrossRef](#)]
59. Pasquini, C.; D’Amario, L.; Zaharieva, I.; Dau, H. Operando Raman spectroscopy tracks oxidation-state changes in an amorphous Co oxide material for electrocatalysis of the oxygen evolution reaction. *J. Chem. Phys.* **2020**, *152*, 194202. [[CrossRef](#)]
60. Ao, K.; Dong, J.; Fan, C.; Wang, D.; Cai, Y.; Li, D.; Huang, F.; Wei, Q. Formation of Yolk-Shelled Nickel–Cobalt Selenide Dodecahedral Nanocages from Metal–Organic Frameworks for Efficient Hydrogen and Oxygen Evolution. *ACS Sustain. Chem. Eng.* **2018**, *6*, 10952–10959. [[CrossRef](#)]
61. Ray, C.; Lee, S.C.; Jin, B.; Kundu, A.; Park, J.H.; Jun, S.C. Stacked Porous Iron-Doped Nickel Cobalt Phosphide Nanoparticle: An Efficient and Stable Water Splitting Electrocatalyst. *ACS Sustain. Chem. Eng.* **2018**, *6*, 6146–6156. [[CrossRef](#)]
62. Sondermann, L.; Jiang, W.; Shviro, M.; Spieß, A.; Woschko, D.; Rademacher, L.; Janiak, C. Nickel-Based Metal–Organic Frameworks as Electrocatalysts for the Oxygen Evolution Reaction (OER). *Molecules* **2022**, *27*, 1241. [[CrossRef](#)] [[PubMed](#)]
63. Hegazy, M.B.Z.; Zander, J.; Weiss, M.; Simon, C.; Gerschel, P.; Sanden, S.A.; Smialkowski, M.; Tetzlaff, D.; Kull, T.; Marschall, R.; et al. FeNi₂S₄ – A Potent Bifunctional Efficient Electrocatalyst for the Overall Electrochemical Water Splitting in Alkaline Electrolyte. *Small* **2024**, *20*, 2311627. [[CrossRef](#)] [[PubMed](#)]
64. Thangasamy, P.; Shanmuganathan, S.; Subramanian, V. A NiCo-MOF nanosheet array based electrocatalyst for the oxygen evolution reaction. *Nanoscale Adv.* **2020**, *2*, 2073–2079. [[CrossRef](#)] [[PubMed](#)]
65. Dutta, S.; Indra, A.; Feng, Y.; Han, H.; Song, T. Promoting electrocatalytic overall water splitting with nanohybrid of transition metal nitride-oxynitride. *Appl. Catal. B Environ.* **2018**, *241*, 521–527. [[CrossRef](#)]
66. Beglau, T.H.Y.; Rademacher, L.; Oestreich, R.; Janiak, C. Synthesis of Ketjenblack Decorated Pillared Ni(Fe) Metal–Organic Frameworks as Precursor Electrocatalysts for Enhancing the Oxygen Evolution Reaction. *Molecules* **2023**, *28*, 4464. [[CrossRef](#)] [[PubMed](#)]
67. Lee, G.; Kim, J. Oxygen evolution catalyst containing CoNi nanoalloy and carbon nanotube maximized the electrochemical surface area and intrinsic activity. *Solid State Sci.* **2023**, *135*. [[CrossRef](#)]
68. Lee, J.-I.; O., S.G.; Kim, Y.J.; Park, S.J.; Sin, G.S.; Kim, J.H.; Ryu, J.H. Electrocatalytic properties of Te incorporated Ni(OH)₂ microcrystals grown on Ni foam. *J. Korean Cryst. Growth Cryst. Technol.* **2021**, *31*, 96–101. [[CrossRef](#)]
69. Park, S.H.; Kang, S.H.; Youn, D.H. Direct One-Step Growth of Bimetallic Ni₂Mo₃N on Ni Foam as an Efficient Oxygen Evolution Electrocatalyst. *Materials* **2021**, *14*, 4768. [[CrossRef](#)]
70. Kanan, M.W.; Nocera, D.G. In Situ Formation of an Oxygen-Evolving Catalyst in Neutral Water Containing Phosphate and Co²⁺. *Science* **2008**, *321*, 1072–1075. [[CrossRef](#)]
71. Gutiérrez-Tarriño, S.; Olloqui-Sariego, J.L.; Calvente, J.J.; Espallargas, G.M.; Rey, F.; Corma, A.; Oña-Burgos, P. Cobalt Metal–Organic Framework Based on Layered Double Nanosheets for Enhanced Electrocatalytic Water Oxidation in Neutral Media. *J. Am. Chem. Soc.* **2020**, *142*, 19198–19208. [[CrossRef](#)]
72. Jeong, D.; Jin, K.; Jerng, S.E.; Seo, H.; Kim, D.; Nahm, S.H.; Kim, S.H.; Nam, K.T. Mn₅O₈ Nanoparticles as Efficient Water Oxidation Catalysts at Neutral pH. *ACS Catal.* **2015**, *5*, 4624–4628. [[CrossRef](#)]
73. Xu, K.; Cheng, H.; Liu, L.; Lv, H.; Wu, X.; Wu, C.; Xie, Y. Promoting Active Species Generation by Electrochemical Activation in Alkaline Media for Efficient Electrocatalytic Oxygen Evolution in Neutral Media. *Nano Lett.* **2016**, *17*, 578–583. [[CrossRef](#)]
74. Jin, K.; Chu, A.; Park, J.; Jeong, D.; Jerng, S.E.; Sim, U.; Jeong, H.-Y.; Lee, C.W.; Park, Y.-S.; Yang, K.D.; et al. Partially Oxidized Sub-10 nm MnO Nanocrystals with High Activity for Water Oxidation Catalysis. *Sci. Rep.* **2015**, *5*, 10279. [[CrossRef](#)]
75. Zaharieva, I.; Chernev, P.; Risch, M.; Klingan, K.; Kohlhoff, M.; Fischer, A.; Dau, H. Electrosynthesis, functional, and structural characterization of a water-oxidizing manganese oxide. *Energy Environ. Sci.* **2012**, *5*, 7081–7089. [[CrossRef](#)]
76. Zhang, X.; Zhang, X.; Xu, H.; Wu, Z.; Wang, H.; Liang, Y. Iron-Doped Cobalt Monophosphide Nanosheet/Carbon Nanotube Hybrids as Active and Stable Electrocatalysts for Water Splitting. *Adv. Funct. Mater.* **2017**, *27*, 1606635. [[CrossRef](#)]
77. Liang, X.; Wang, S.; Feng, J.; Xu, Z.; Guo, Z.; Luo, H.; Zhang, F.; Wen, C.; Feng, L.; Wan, C.; et al. Structural transformation of metal–organic frameworks and identification of electrocatalytically active species during the oxygen evolution reaction under neutral conditions. *Inorg. Chem. Front.* **2023**, *10*, 2961–2977. [[CrossRef](#)]
78. Jin, K.; Park, J.; Lee, J.; Yang, K.D.; Pradhan, G.K.; Sim, U.; Jeong, D.; Jang, H.L.; Park, S.; Kim, D.; et al. Hydrated manganese(II) phosphate (Mn₃(PO₄)₂·3H₂O) as a water oxidation catalyst. *J. Am. Chem. Soc.* **2014**, *136*, 7435–7443. [[CrossRef](#)]
79. Wang, N.; Cao, Z.; Zheng, X.; Zhang, B.; Kozlov, S.M.; Chen, P.; Zou, C.; Kong, X.; Wen, Y.; Liu, M.; et al. Hydration-Effect-Promoting Ni–Fe Oxyhydroxide Catalysts for Neutral Water Oxidation. *Adv. Mater.* **2020**, *32*, 1906806. [[CrossRef](#)]
80. Khirak, B.N.; Hasanzadeh, M.; Simchi, A. Electrocatalytic hydrogen evolution reaction on graphene supported transition metal-organic frameworks. *Inorg. Chem. Commun.* **2021**, *127*, 108525. [[CrossRef](#)]
81. Duraisamy, S.; Ganguly, A.; Sharma, P.K.; Benson, J.; Davis, J.; Papakonstantinou, P. One-Step Hydrothermal Synthesis of Phase-Engineered MoS₂/MoO₃ Electrocatalysts for Hydrogen Evolution Reaction. *ACS Appl. Nano Mater.* **2021**, *4*, 2642–2656. [[CrossRef](#)]

82. Sannasi, V.; Thangasamy, P.; Raj, J.A.; Sathish, M. Transformation of sluggish higher valent molybdenum into electro-catalytically active amorphous carbon doped MoO₂/MoO_{3-x} nanostructures using phyllanthus reticulatus fruit extract as natural reducing agent in supercritical fluid processing. *Int. J. Hydrog. Energy* **2019**, *44*, 21692–21702. [CrossRef]
83. Hu, C.; Dai, L. Multifunctional Carbon-Based Metal-Free Electrocatalysts for Simultaneous Oxygen Reduction, Oxygen Evolution, and Hydrogen Evolution. *Adv Mater* **2017**, *29*, 1604942. [CrossRef] [PubMed]
84. Kumar, J.S.; Bolar, S.; Murmu, N.C.; Ganesh, R.S.; Inokawa, H.; Banerjee, A.; Kuila, T. Synthesis of Tri-functional Core-shell CuO@carbon Quantum Dots@carbon Hollow Nanospheres Heterostructure for Non-enzymatic H₂O₂ Sensing and Overall Water Splitting Applications. *Electroanalysis* **2019**, *31*, 2120–2129. [CrossRef]
85. Zhang, G.; Wang, J.; Xie, Y.; Shao, Y.; Ling, Y.; Chen, Y.; Zhang, Y. CoS₂ particles loaded on MOF-derived hollow carbon spheres with enhanced overall water splitting. *Electrochimica Acta* **2023**, *458*, 142511. [CrossRef]
86. Liu, M.; Zheng, W.; Ran, S.; Boles, S.T.; Lee, L.Y.S. Overall Water-Splitting Electrocatalysts Based on 2D CoNi-Metal-Organic Frameworks and Its Derivative. *Adv. Mater. Interfaces* **2018**, *5*, 1800849. [CrossRef]
87. Arunkumar, P.; Gayathri, S.; Han, J.H. Impact of an Incompatible Atomic Nickel-Incorporated Metal–Organic Framework on Phase Evolution and Electrocatalytic Activity of Ni-Doped Cobalt Phosphide for the Hydrogen Evolution Reaction. *ACS Appl. Energy Mater.* **2022**, *5*, 2975–2992. [CrossRef]
88. Zhu, D.; Liu, J.; Zhao, Y.; Zheng, Y.; Qiao, S.Z. Engineering 2D Metal–Organic Framework/MoS₂ Interface for Enhanced Alkaline Hydrogen Evolution. *Small* **2019**, *15*, 1805511. [CrossRef]
89. Nady, H.; El-Rabiei, M.; Deyab, M.; Samy, M.; El-Hafez, G.M.A. Ni–Cr alloys for effectively enhancing hydrogen evolution processes in phosphate-buffered neutral electrolytes. *Int. J. Hydrog. Energy* **2022**, *47*, 39030–39046. [CrossRef]
90. Tian, J.; Liu, Q.; Asiri, A.M.; Sun, X. Self-Supported Nanoporous Cobalt Phosphide Nanowire Arrays: An Efficient 3D Hydrogen-Evolving Cathode over the Wide Range of pH 0–14. *J. Am. Chem. Soc.* **2014**, *136*, 7587–7590. [CrossRef]
91. Chen, M.; Qi, J.; Zhang, W.; Cao, R. Electrosynthesis of NiP_x nanospheres for electrocatalytic hydrogen evolution from a neutral aqueous solution. *Chem. Commun.* **2017**, *53*, 5507–5510. [CrossRef]
92. Li, K.; Zhang, J.; Wu, R.; Yu, Y.; Zhang, B. Anchoring CoO Domains on CoSe₂ Nanobelts as Bifunctional Electrocatalysts for Overall Water Splitting in Neutral Media. *Adv. Sci.* **2016**, *3*, 1500426. [CrossRef]
93. Wu, R.; Xiao, B.; Gao, Q.; Zheng, Y.R.; Zheng, X.S.; Zhu, J.F.; Gao, M.R.; Yu, S.H. A Janus Nickel Cobalt Phosphide Catalyst for High-Efficiency Neutral-pH Water Splitting. *Angew. Chem. Int. Ed.* **2018**, *57*, 15445–15449. [CrossRef]
94. Feng, J.X.; Xu, H.; Ye, S.H.; Ouyang, G.; Tong, Y.X.; Li, G.R. Silica–Polypyrrole Hybrids as High-Performance Metal-Free Electrocatalysts for the Hydrogen Evolution Reaction in Neutral Media. *Angew. Chem. Int. Ed.* **2017**, *56*, 8120–8124. [CrossRef]
95. Zhao, S.; Xie, R.; Kang, L.; Yang, M.; He, X.; Li, W.; Wang, R.; Brett, D.J.L.; He, G.; Chai, G.; et al. Enhancing Hydrogen Evolution Electrocatalytic Performance in Neutral Media via Nitrogen and Iron Phosphide Interactions. *Small Sci.* **2021**, *1*, 2100032. [CrossRef]
96. Wang, K.; Si, Y.; Lv, Z.; Yu, T.; Liu, X.; Wang, G.; Xie, G.; Jiang, L. Efficient and stable Ni–Co–Fe–P nanosheet arrays on Ni foam for alkaline and neutral hydrogen evolution. *Int. J. Hydrog. Energy* **2020**, *45*, 2504–2512. [CrossRef]
97. Fan, Y.; Sun, Y.; Zhang, X.; Guo, J. Synergistic effect between sulfur and CoFe alloys embedded in N-doped carbon nanosheets for efficient hydrogen evolution under neutral condition. *Chem. Eng. J.* **2021**, *426*, 131922. [CrossRef]
98. Zheng, J.; Zhang, J.; Zhang, L.; Zhang, W.; Wang, X.; Cui, Z.; Song, H.; Liang, Z.; Du, L. Ultrafast Carbothermal Shock Constructing Ni₃Fe_{1-x}Cr_x Intermetallic Integrated Electrodes for Efficient and Durable Overall Water Splitting. *ACS Appl. Mater. Interfaces* **2022**, *14*, 19524–19533. [CrossRef]
99. Woo, S.; Lee, J.; Lee, D.S.; Kim, J.K.; Lim, B. Electrospun Carbon Nanofibers with Embedded Co-Ceria Nanoparticles for Efficient Hydrogen Evolution and Overall Water Splitting. *Materials* **2020**, *13*, 856. [CrossRef]
100. Yang, H.; Zhou, Z.; Yu, H.; Wen, H.; Yang, R.; Peng, S.; Sun, M.; Yu, L. Alkali treatment of layered double hydroxide nanosheets as highly efficient bifunctional electrocatalysts for overall water splitting. *J. Colloid Interface Sci.* **2023**, *636*, 11–20. [CrossRef]
101. Moi, C.T.; Sahu, A.; Qureshi, M. Tapping the Potential of High-Valent Mo and W Metal Centers for Dynamic Electronic Structures in Multimetallic FeVO(OH)/Ni(OH)₂ for Ultrastable and Efficient Overall Water Splitting. *ACS Appl. Mater. Interfaces* **2023**, *15*, 5336–5344. [CrossRef] [PubMed]
102. Ge, K.; Zhang, Y.; Zhao, Y.; Zhang, Z.; Wang, S.; Cao, J.; Yang, Y.; Sun, S.; Pan, M.; Zhu, L. Room Temperature Preparation of Two-Dimensional Black Phosphorus@Metal Organic Framework Heterojunctions and Their Efficient Overall Water-Splitting Electrocatalytic Reactions. *ACS Appl. Mater. Interfaces* **2022**, *14*, 31502–31509. [CrossRef] [PubMed]
103. Liu, B.; Li, S.; Wang, T.; Yang, Y.; Wang, L.; Zhang, X.; Liu, Z.; Niu, L. Construction of CoFe bimetallic phosphide micro-flowers electrocatalyst for highly efficient overall water splitting. *Catal. Commun.* **2023**, *175*, 106607. [CrossRef]
104. Chai, N.; Kong, Y.; Liu, T.; Ying, S.; Jiang, Q.; Yi, F.-Y. (FeMnCe)-co-doped MOF-74 with significantly improved performance for overall water splitting. *Dalton Trans.* **2023**, *52*, 11601–11610. [CrossRef]

Disclaimer/Publisher’s Note: The statements, opinions and data contained in all publications are solely those of the individual author(s) and contributor(s) and not of MDPI and/or the editor(s). MDPI and/or the editor(s) disclaim responsibility for any injury to people or property resulting from any ideas, methods, instructions or products referred to in the content.